Charged pion electric polarizability from four-point functions in lattice QCD

Frank X. Lee,[1,*] Andrei Alexandru,[1,2,†] Chris Culver,[3,‡] and Walter Wilcox[4,§]

[1]*Physics Department, The George Washington University, Washington, District of Columbia 20052, USA*
[2]*Department of Physics, University of Maryland, College Park, Maryland 20742, USA*
[3]*Department of Mathematical Sciences, University of Liverpool, Liverpool L69 7ZL, United Kingdom*
[4]*Department of Physics, Baylor University, Waco, Texas 76798, USA*

(Received 17 January 2023; revised 31 May 2023; accepted 11 July 2023; published 24 July 2023)

Polarizabilities reveal valuable information on the internal structure of hadrons in terms of charge and current distributions. For neutral hadrons, the standard approach is the background field method, but for a charged hadron, its acceleration under the applied field complicates the isolation of the polarization energy. In this work, we explore an alternative method based on four-point functions in lattice QCD. The approach offers a transparent picture on how polarizabilities arise from photon, quark, and gluon interactions. We carry out a proof-of-concept simulation on the electric polarizability of a charged pion, using quenched Wilson action on a $24^3 \times 48$ lattice at $\beta = 6.0$ with pion mass from 1100 MeV to 370 MeV. We show in detail the evaluation and analysis of the four-point correlation functions and report results on charge radius and electric polarizability. Our results from connected diagrams suggest that charged pion α_E is due to a cancellation between elastic and inelastic contributions. It would be interesting to see how the cancellation plays out at smaller pion masses in future simulations.

DOI: 10.1103/PhysRevD.108.014512

I. INTRODUCTION

Understanding electromagnetic polarizabilities has been a long-term goal of lattice QCD. The challenge in the effort lies in the need to apply both QCD and QED principles. The standard approach to compute polarizabilities is the background field method which has been widely used for dipole polarizabilities [1–19]. Methods to study higher-order polarizabilities have also been proposed [20–23] in this approach. Although such calculations are relatively straightforward, requiring only energy shifts from two-point functions, there are a number of unique challenges. First, since weak fields are needed, the energy shift involved is very small relative to the mass of the hadron (on the order of one part in a million depending on the field strength). This challenge has been successfully overcome by relying on statistical correlations with or without the field. Second, there is the issue of discontinuities across the boundaries when applying a uniform field on a periodic lattice. This has been largely resolved by using quantized values for the fields, or Dirichlet boundary conditions. Third and more importantly, a charged hadron accelerates in an electric field and exhibits Landau levels in a magnetic field. Such motions are unrelated to polarizability and must be disentangled from the deformation energy on which the polarizabilities are defined. For this reason, most calculations have focused on neutral hadrons. For charged hadrons, what happens is that the two-point correlator does not develop single exponential behavior at large times. In Ref. [24], a relativistic propagator for a charged scalar is used to demonstrate how to fit such lattice data for charged pions and kaons. This approach is improved recently in Ref. [25] with an effective charged scalar propagator exactly matching the lattice being used to generate the lattice QCD data. A new fitting procedure is proposed where a χ^2-function utilizes information in both the real and imaginary parts of the correlator while remaining invariant under gauge transformations of the background field. For magnetic polarizability, a field-dependent quark-propagator eigenmode projector is used to filter out the effects of Landau levels [26,27]. These special techniques for charged particles involve fairly complicated analysis to treat the collective motion of the system in order to isolate the polarizabilities.

In this work, we explore an alternative approach based on four-point functions in lattice QCD. Instead of background fields, electromagnetic currents couple to quark fields to induce interactions to all orders. It is a general approach that

*fxlee@gwu.edu
†aalexan@gwu.edu
‡C.Culver@liverpool.ac.uk
§walter_wilcox@baylor.edu

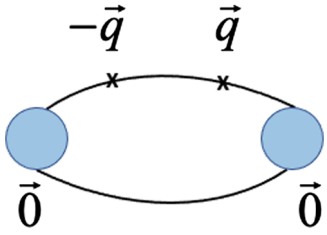

FIG. 1. Four-point function for charged pion polarizabilities under the zero-momentum Breit frame. Time flows from right to left and the four momentum conservation is expressed as $p_2 = q_2 + q_1 + p_1$.

treats neutral and charged particles on equal footing, but particularly suited for charged particles. The trade-off is an increased computational demand of four-point functions. Although four-point functions have been applied to study various aspects of hadron structure [28–33], not too much attention has been paid to its potential application for polarizabilities. We know of two such studies from a long time ago [34,35], a recent calculation on the pion [36], and a preliminary one on the proton [37]. A reexamination of the formalism in Ref. [35] is recently carried out in Ref. [38] for both electric and magnetic polarizabilities of a charged pion and a proton. We also note that although Refs. [11,21] are based on the background field method, they are in fact four-point function calculations. A perturbative expansion in the background field at the action level is performed in which two vector current insertions couple the background field to the hadron correlation function, leading to the same diagrammatic structures as in this work.

Experimentally, polarizabilities are primarily studied by low-energy Compton scattering. Theoretically, a variety of methods have been employed to describe the physics involved, from the quark-confinement model [39], to the Nambu-Jona-Lasinio model [40,41], to the linear sigma model [42], to dispersion relations [43–46], to chiral perturbation theory (ChPT) [47–49] and chiral effective field theory (EFT) [50,51]. Reviews on hadron polarizabilities can be found in Refs. [47,51,52].

The presentation is organized as follows. In Sec. II we outline the methodology to extract polarizabilities, using the electric polarizability of a charged pion as an example. In Sec. III we detail our notations and algorithms used to evaluate the four-point functions, including how the sequential-source technique (SST) can be applied in this context. In Sec. IV we show our analysis procedure and results from a proof-of-concept simulation. In Sec. V we give concluding remarks and an outlook. Some technical details are put in the Appendixes.

II. METHODOLOGY

In Ref. [38], a formula is derived for electric polarizability of a charged pion,

$$\alpha_E = \frac{\alpha\langle r_E^2\rangle}{3m_\pi} + \lim_{\boldsymbol{q}\to 0}\frac{2\alpha}{\boldsymbol{q}^2}\int_0^\infty dt\left[Q_{44}(\boldsymbol{q},t) - Q_{44}^{\mathrm{elas}}(\boldsymbol{q},t)\right]. \quad (1)$$

Here $\alpha = 1/137$ is the fine structure constant. The first term in the formula involves the charge radius and pion mass (we will refer to this term as the elastic contribution). The second term has the elastic contribution Q_{44}^{elas} subtracted from the total (we will refer to this term as the inelastic contribution). The formula will be used in discrete Euclidean spacetime but we keep the Euclidean time axis continuous for notational convenience. Special kinematics (called zero-momentum Breit frame) are employed in the formula to mimic low-energy Compton scattering. The process is illustrated in Fig. 1, where the initial (p_1) and final (p_2) pions are at rest and the photons have purely spacelike momentum,

$$p_1 = (\boldsymbol{0}, m_\pi), \quad q_1 = (\boldsymbol{q}, 0), \quad q_2 = (-\boldsymbol{q}, 0), \quad p_2 = (\boldsymbol{0}, m_\pi). \quad (2)$$

The Q_{44} is defined as the $\mu = 4 = \nu$ component of the Fourier transforms,

$$Q_{\mu\nu}(\boldsymbol{q}, t_2, t_1) \equiv \sum_{\boldsymbol{x}_2,\boldsymbol{x}_1} e^{-i\boldsymbol{q}\cdot\boldsymbol{x}_2} e^{i\boldsymbol{q}\cdot\boldsymbol{x}_1} P_{\mu\nu}(\boldsymbol{x}_2, \boldsymbol{x}_1, t_3, t_2, t_1, t_0), \quad (3)$$

where $P_{\mu\nu}$ is a four-point function defined in position space (Ω denotes the vacuum),

$$P_{\mu\nu}(\boldsymbol{x}_2, \boldsymbol{x}_1, t_3, t_2, t_1, t_0) \equiv \frac{\sum_{\boldsymbol{x}_3,\boldsymbol{x}_0}\langle\Omega|\psi(x_3) : j_\mu^L(x_2) j_\nu^L(x_1) : \psi^\dagger(x_0)|\Omega\rangle}{\sum_{\boldsymbol{x}_3,\boldsymbol{x}_0}\langle\Omega|\psi(x_3)\psi^\dagger(x_0)|\Omega\rangle}. \quad (4)$$

Here ψ is the interpolating field of the pion and j_μ^L the lattice version of the electromagnetic current density. The two-point function in the denominator is for normalization. Normal ordering is used to include the required subtraction of vacuum expectation values (VEV) on the lattice. The sums over $\boldsymbol{x}_0$ and $\boldsymbol{x}_3$ enforce zero-momentum pions at the source (t_0) and sink (t_3). The two currents are inserted at t_1 and t_2 with two possibilities of time ordering implied in the normal ordering. The field operators for ψ and j_μ^L used in this work, along with conservation properties of Q_{44} at $\boldsymbol{q} = 0$, are given in Appendix A. To see the structure of the four-point function in Eq. (4), we insert a complete set of states in the numerator (twice) and in the denominator (once). When the times are well separated (defined by the time limits $t_3 \gg t_{1,2} \gg t_0$) the correlator is dominated by the ground state,

$$
\begin{aligned}
&P_{\mu\nu}(\boldsymbol{x}_2, \boldsymbol{x}_1, t_3, t_2, t_1, t_0) \\
&\to \frac{N_s^2 |\langle \pi(\mathbf{0})|\psi(0)|\Omega\rangle|^2 e^{-m_\pi t_3} \langle \pi(\mathbf{0})| : j_\mu^L(x_2) j_\nu^L(x_1) : |\pi(\mathbf{0})\rangle}{N_s^2 |\langle \pi(\mathbf{0})|\psi(0)|\Omega\rangle|^2 e^{-m_\pi t_3}} \\
&\to \langle \pi(\mathbf{0})| : j_\mu^L(x_2) j_\nu^L(x_1) : |\pi(\mathbf{0})\rangle \\
&= \langle \pi(\mathbf{0})| T j_\mu^L(x_2) j_\nu^L(x_1) |\pi(\mathbf{0})\rangle - \langle \Omega| T j_\mu^L(x_2) j_\nu^L(x_1) |\Omega\rangle.
\end{aligned} \tag{5}
$$

Here $N_s = N_x N_y N_z$ is the number of spatial sites on the lattice. The role of the two-point function as normalization and the inclusion of VEV subtraction is evident in the limit.

Assuming time separation $t = t_2 - t_1 > 0$ and inserting a complete set of intermediate states, the diagonal component of $Q_{\mu\nu}$ develops the time dependence in the same limits,

$$
\begin{aligned}
Q_{\mu\mu}(\boldsymbol{q}, t) = N_s^2 \sum_n |\langle \pi(\mathbf{0})| j_\mu^L(0) |n(\boldsymbol{q})\rangle|^2 e^{-a(E_n - m_\pi)t} \\
- N_s^2 \sum_n |\langle \Omega| j_\mu^L(0) |n(\boldsymbol{q})\rangle|^2 e^{-aE_n t}.
\end{aligned} \tag{6}
$$

At large time separations, it is dominated by the elastic contribution ($n = \pi$ term in the first sum),

$$
Q_{\mu\mu}^{\text{elas}}(\boldsymbol{q}, t) \equiv N_s^2 |\langle \pi(\mathbf{0})| j_\mu^L(0) |\pi(\boldsymbol{q})\rangle|^2 e^{-a(E_\pi - m_\pi)t}. \tag{7}
$$

We see that the elastic piece in the four-point function has information on the form factor of the pion through the amplitude squared. The form factor F_π can be determined from Q_{44} at large time separations,

$$
Q_{44}^{\text{elas}}(\boldsymbol{q}, t) = \frac{(E_\pi + m_\pi)^2}{4 E_\pi m_\pi} F_\pi^2(\boldsymbol{q}^2) e^{-a(E_\pi - m_\pi)t}. \tag{8}
$$

The charge radius $\langle r_E^2 \rangle$ in the formula can then be extracted from F_π. A salient feature here is that the elastic contribution in four-point functions is positive definite.

Aside from the charge radius term in Eq. (1), α_E is proportional to the difference in the areas under the Q_{44} and Q_{44}^{elas} curves. It is this difference that is responsible for the sign of α_E^π. On a finite lattice the time integral does not really extend to ∞, but are limited to the available time slices between the two current insertions. In practice, one should check if the largest time separation is enough to establish the elastic limit. Equivalent directions for $\boldsymbol{q}$ can be used to improve the signal-to-noise ratio. Note that α_E has the expected physical unit of a^3 (fm^3) since $1/\boldsymbol{q}^2$ scales like a^2, the integral scales like a, and Q_{44} is dimensionless in our notation.

III. CORRELATION FUNCTIONS

In this section, we detail how to simulate Eq. (4) and its Fourier transform Eq. (3) at the quark level. Wick contractions of quark-antiquark pairs in the unsubtracted part lead to topologically distinct quark-line diagrams shown in Fig. 2. The raw correlation functions can be found in Appendix B.

Diagrams (a), (b), and (c) are connected. Diagram (d) has a loop that is disconnected from the hadron, but connected between the two currents. Diagram (e) has one disconnected loop and diagram (f) has two such loops. Furthermore, diagrams (d), (e), and (f) must have associated VEV subtracted. However, if conserved lattice current density is used, there is no need for subtraction in diagram (e) since the VEV vanishes in the configuration average [53]. In this work, we focus on the connected contributions [diagrams (a), (b), and (c)]. The disconnected contributions [diagrams (d), (e), and (f)] are more challenging and are left for future

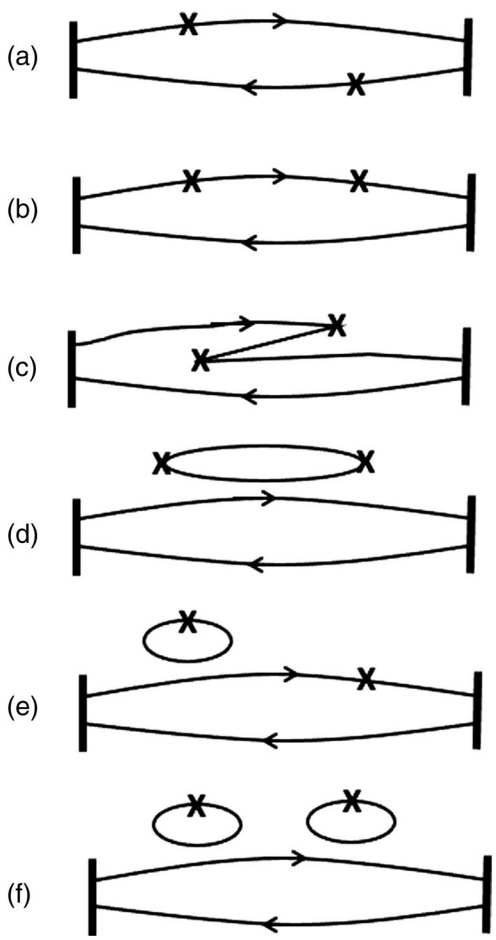

FIG. 2. Skeleton diagrams of a four-point function contributing to polarizabilities of a meson: (a) connected insertion: different flavor, (b) connected insertion: same flavor, (c) connected insertion: same flavor Z-graph, (d) disconnected insertion: single loop, double current, (e) disconnected insertion: single loop, (f) disconnected insertion: double loop. In each diagram, flavor permutations are assumed as well as gluon lines that connect the quark lines. The zero-momentum pion interpolating fields are represented by vertical bars (wall sources). Time flows from right to left.

work. In particular, we will explain how to use the sequential source technique (SST) to simplify the evaluations.

A. Two-point functions

First, we show how to evaluate the two-point function in Eq. (4) which serves as normalization for the four-point functions. It has the following Wick contraction using the interpolating operator in Eq. (A1),

$$\sum_{\boldsymbol{x}_3,\boldsymbol{x}_0}\langle\Omega|\psi(x_3)\psi^\dagger(x_0)|\Omega\rangle=\sum_{\boldsymbol{x}_3,\boldsymbol{x}_0}\mathrm{Tr}_{s,c}\Big[\gamma_5 S_d(x_0,x_3)\gamma_5 S_u(x_3,x_0)\Big], \tag{9}$$

where S_q denotes a quark propagator that carries the full spacetime and spin and color information between two points.[1] The double sum projects to zero momentum both at the source x_0 and the sink x_3 as required by the special kinematics. The full evaluation involves essentially all-to-all propagation which is computationally prohibitive. Instead, we employ wall sources without gauge fixing as an approximation, with the expectation that gauge-dependent contributions to the final observables will vanish in the configuration average [30,54]. Only terms in the double sum where the quarks are at the same location form the signal, the rest contribute to noise. Details of our implementation of the wall source can be found in Appendix C.

If we insert the wall at time slice t_0 and project to zero momentum at t_3 in Eq. (9), we have

$$\begin{aligned}&\sum_{\boldsymbol{x}_3,\boldsymbol{x}_0}\langle\Omega|\psi(x_3)\psi^\dagger(x_0)|\Omega\rangle\\&=\mathrm{Tr}_{s,c}\Big[\mathcal{W}^T\gamma_5 S_d(x_0,x_3)\gamma_5 S_u(x_3,x_0)\mathcal{W}\Big]\\&=\mathrm{Tr}_{s,c}\Big[\mathcal{W}^T\gamma_5 P(t_0)M_d^{-1}P(t_3)^T\gamma_5 P(t_3)M_u^{-1}P(t_0)^T\mathcal{W}\Big].\end{aligned} \tag{10}$$

The symbols $\mathcal{W}$ and $P(t)$ are defined in Appendix C. We introduce two zero-momentum quark propagators called $a1$ and $a2$ emanating from the walls at t_0 and t_3, respectively,

$$V_{a1}^{(q)}\equiv M_q^{-1}P(t_0)^T\mathcal{W},\qquad V_{a2}^{(q)}\equiv M_q^{-1}P(t_3)^T\mathcal{W}. \tag{11}$$

We use "V" to emphasize that the wall-to-point quark propagators so defined are column vectors in the $(\boldsymbol{x},s,c)$ space. Using $a1$, the two-point function can be written as

$$\begin{aligned}&\sum_{\boldsymbol{x}_3,\boldsymbol{x}_0}\langle\Omega|\psi(x_3)\psi^\dagger(x_0)|\Omega\rangle\\&=\mathrm{Tr}_{s,c}\Big[\Big(P(t_3)\gamma_5 V_{a1}^{(d)}\Big)^\dagger\Big(P(t_3)\gamma_5 V_{a1}^{(u)}\Big)\Big]\\&=\mathrm{Tr}_{s,c}\Big[\Big(P(t_3)V_{a1}^{(d)}\Big)^\dagger\Big(P(t_3)V_{a1}^{(u)}\Big)\Big]\quad(\textbf{Type 1}).\end{aligned} \tag{12}$$

In the last step the γ_5-hermiticity of M_q^{-1} is used to eliminate γ_5. Similarly, if we insert the wall at time slice t_3 and project to zero momentum at t_0, we get in terms of $a2$,

$$\begin{aligned}&\sum_{\boldsymbol{x}_3,\boldsymbol{x}_0}\langle\Omega|\psi(x_3)\psi^\dagger(x_0)|\Omega\rangle\\&=\mathrm{Tr}_{s,c}\Big[\Big(P(t_0)\gamma_5 V_{a2}^{(u)}\Big)^\dagger\Big(P(t_0)\gamma_5 V_{a2}^{(d)}\Big)\Big]\\&=\mathrm{Tr}_{s,c}\Big[\Big(P(t_0)V_{a2}^{(u)}\Big)^\dagger\Big(P(t_0)V_{a2}^{(d)}\Big)\Big]\quad(\textbf{Type 2}).\end{aligned} \tag{13}$$

If we insert two walls, one at t_0, one at t_3, we obtain additional expressions,

$$\begin{aligned}&\sum_{\boldsymbol{x}_3,\boldsymbol{x}_0}\langle\Omega|\psi(x_3)\psi^\dagger(x_0)|\Omega\rangle\\&=\mathrm{Tr}_{s,c}\Big[\mathcal{W}^T\gamma_5 S_d(x_0,x_3)\mathcal{W}\mathcal{W}^T\gamma_5 S_u(x_3,x_0)\mathcal{W}\Big]\\&=\mathrm{Tr}_{s,c}\Big[\Big(\mathcal{W}^T P(t_3)V_{a1}^{(d)}\Big)^\dagger\Big(\mathcal{W}^T P(t_3)V_{a1}^{(u)}\Big)\Big]\\&=\mathrm{Tr}_{s,c}\Big[\Big(\mathcal{W}^T P(t_0)V_{a2}^{(u)}\Big)^\dagger\Big(\mathcal{W}^T P(t_0)V_{a2}^{(d)}\Big)\Big]\quad(\textbf{Type 3}).\end{aligned} \tag{14}$$

The expressions in the above three equations (which we denote as Type 1, 2, 3 as indicated) are different estimators of the wall-to-wall two-point function with zero momentum for both initial and final pions. They are expected to approach the same value in the limit of infinite number of configurations. In the following, we use our notation to evaluate the connected four-point functions in Fig. 2.

B. Four-point functions

We start with local (or point) current insertions of four-point functions which have relatively simple Wick contractions. The results in this work will be based on conserved (or point-split) currents which avoids the issue of computing the renormalization constant Z_V for vector currents. Below we detail how to evaluate the connected contributions using both local and conserved currents.

1. Diagram a (different flavor)

There are two terms, d_4 and d_2 in Eq. (B4), that are contributing to the connected part of diagram a. They are characterized by the charge factor $q_u q_{\bar{d}}=2/9$. The two terms are related by a flavor permutation ($1\leftrightarrow 2$ switch).

[1]In this work, all correlation functions in such expressions are understood as path integral expectation values in lattice QCD. They are evaluated as averages over gauge configurations in Monte Carlo simulations.

Under isospin symmetry in u and d quarks, the two terms have equal contributions. Including the Fourier transforms and setting $\mu = 4 = \nu$ for electric polarizability, the correlation function can be written as[2]

$$\tilde{Q}_{44}^{(a,\mathrm{PC})} = -\frac{4}{9} Z_V^2 \kappa^2 \mathrm{Tr}_{s,c}\Big[\gamma_5 S(t_0,t_2)\gamma_4 e^{-i\boldsymbol{q}} S(t_2,t_3)\gamma_5 S(t_3,t_1)\gamma_4 e^{i\boldsymbol{q}} S(t_1,t_0)\Big]. \tag{15}$$

We evaluate the correlation function by inserting two walls, one at t_0 and one at t_3,

$$\begin{aligned}\tilde{Q}_{44}^{(a,\mathrm{PC})}(\boldsymbol{q},t_1,t_2) &= -\frac{4}{9} Z_V^2 \kappa^2 \mathrm{Tr}_{s,c}\Big[\mathcal{W}^T\gamma_5 S(t_0,t_2) e^{-i\boldsymbol{q}}\gamma_4 S(t_2,t_3)\mathcal{W}\mathcal{W}^T\gamma_5 S(t_3,t_1) e^{i\boldsymbol{q}}\gamma_4 S(t_1,t_0)\mathcal{W}\Big] \\ &= -\frac{4}{9} Z_V^2 \kappa^2 \mathrm{Tr}_{s,c}\Big[\mathcal{W}^T\gamma_5 P(t_0) M_q^{-1} P(t_2)^T e^{-i\boldsymbol{q}}\gamma_4 P(t_2) M_q^{-1} P(t_3)^T \mathcal{W} \\ &\quad \times \mathcal{W}^T\gamma_5 P(t_3) M_q^{-1} P(t_1)^T e^{i\boldsymbol{q}}\gamma_4 P(t_1) M_q^{-1} P(t_0)^T \mathcal{W}\Big]. \end{aligned} \tag{16}$$

The notation makes it clear that all spatial sums are automatically incorporated into the matrix multiplications. Using the V_{a1} and V_{a2} propagators defined in Eq. (11) and the γ_5-hermiticity of M^{-1}, the final expression for diagram (a) can be written as

$$\tilde{Q}_{44}^{(a,\mathrm{PC})}(\boldsymbol{q},t_1,t_2) = \frac{4}{9} Z_V^2 \kappa^2 \mathrm{Tr}_{s,c}\Big[\Big([P(t_2)V_{a2}]^\dagger\gamma_5\gamma_4 e^{i\boldsymbol{q}} P(t_2) V_{a1}\Big)^\dagger \Big([P(t_1)V_{a2}]^\dagger\gamma_5\gamma_4 e^{i\boldsymbol{q}} P(t_1) V_{a1}\Big)\Big]. \tag{17}$$

There is an overall sign change from taking the dagger. The first parenthesis corresponds to the current insertion at t_2 on one of the quark lines in the pion; the second parenthesis the current insertion at t_1 on the other quark line. Both t_1 and t_2 are free to vary between t_0 and t_3.

In the case of conserved current, there are 8 terms contributing to diagram (a) in Eq. (B6). Their sum under isospin symmetry, along with the Fourier transforms and wall-source insertions, can be written in similar form,

$$\begin{aligned}\tilde{Q}_{44}^{(a,\mathrm{PS})}(\boldsymbol{q},t_1,t_2) &= \frac{1}{9}\kappa^2(d_{16}+d_{18}+d_{20}+d_{22}+d_8+d_{10}+d_{12}+d_{14}) \\ &= \frac{4}{9}\kappa^2 \mathrm{Tr}_{s,c}\Big[\Big([P(t_2)V_{a2}]^\dagger\gamma_5(1-\gamma_4) e^{i\boldsymbol{q}} U_4(t_2,t_2+1) P(t_2+1) V_{a1} \\ &\quad - [P(t_2+1)V_{a2}]^\dagger\gamma_5(1+\gamma_4) U_4^\dagger(t_2+1,t_2) e^{i\boldsymbol{q}} P(t_2) V_{a1}\Big)^\dagger \\ &\quad \times \Big([P(t_1)V_{a2}]^\dagger\gamma_5(1-\gamma_4) e^{i\boldsymbol{q}} U_4(t_1,t_1+1) P(t_1+1) V_{a1} \\ &\quad - [P(t_1+1)V_{a2}]^\dagger\gamma_5(1+\gamma_4) U_4^\dagger(t_1+1,t_1) e^{i\boldsymbol{q}} P(t_1) V_{a1}\Big)\Big], \end{aligned} \tag{18}$$

with local current replaced by its point-split form in the parentheses.

2. Diagram (b) (same flavor) and SST

For local current, there are 2 terms, d_1 and d_7 in Eq. (B4), that are contributing to the connected part of same-flavor correlations. They are characterized by the charge factors $q_u q_u = 4/9$ or $q_{\bar{d}} q_{\bar{d}} = 1/9$. The d_1 diagram is clockwise propagation $t_0 \to t_3 \to t_2 \to t_1 \to t_0$ where the two currents couple to the same u quark, while the d_7 diagram is counterclockwise propagation $t_0 \to t_1 \to t_2 \to t_3 \to t_0$ where the two currents couple to the same d quark. Under isospin symmetry, the total contribution from uu and dd correlations has a total charge factor of $4/9 + 1/9 = 5/9$.

Including the Fourier transforms, setting $\mu = 4 = \nu$ for electric polarizability, and inserting the wall sources, the correlation function can be written as

$$\tilde{Q}_{44}^{(b,\mathrm{PC})} = \frac{5}{9} Z_V^2 \kappa^2 \mathrm{Tr}_{s,c}\Big[\mathcal{W}^T\gamma_5 S(t_0,t_1)\gamma_4 e^{i\boldsymbol{q}} S(t_1,t_2)\gamma_4 e^{-i\boldsymbol{q}} S(t_2,t_3)\mathcal{W}\mathcal{W}^T\gamma_5 S(t_3,t_0)\mathcal{W}\Big]. \tag{19}$$

[2]We use $Q_{\mu\nu}$ for normalized correlation functions as defined in Eqs. (3) and (4), and tilded $\tilde{Q}_{\mu\nu}$ for unnormalized, i.e., without the denominator Eq. (4).

This expression involves numerous quark propagators; t_0 and t_3 are fixed, but t_1 and t_2 are free to vary. To cut down the computational cost, we fix the current at t_1. Then only one new inversion between t_1 and t_2 is required. Since the current insertions take place between the hadron source (t_0) and sink (t_3), a method called SST (sequential source technique) can be employed for the propagator. To see how SST arises in this context, we first define the product that involves $t_0 \to t_3 \to t_2$ propagation as

$$\begin{aligned}
&\gamma_4 e^{-iq} S(t_2,t_3)\mathcal{W}\mathcal{W}^T\gamma_5 S(t_3,t_0)\mathcal{W} \\
&= \gamma_4 e^{-iq} P(t_2) M_q^{-1} P(t_3)^T \mathcal{W}\mathcal{W}^T\gamma_5 P(t_3) M_q^{-1} P(t_0)^T \mathcal{W} \\
&= \gamma_4 e^{-iq} P(t_2) V_{a2} \mathcal{W}^T P(t_3)\gamma_5 V_{a1}, \qquad (20)
\end{aligned}$$

which is built directly from the two previously-computed propagators V_{a1} and V_{a2} along with other factors. This does not require a new inversion. Next, we define the rest in Eq. (19) as

$$\begin{aligned}
&\mathcal{W}^T\gamma_5 S(t_0,t_1)\gamma_4 e^{iq} S(t_1,t_2) \\
&= \mathcal{W}^T\gamma_5 P(t_0) M_q^{-1} P(t_1)^T \gamma_4 e^{iq} P(t_1) M_q^{-1} P(t_2)^T \\
&= \left[P(t_2)\gamma_5 M_q^{-1}\gamma_5 P(t_1)^T \gamma_4 e^{-iq} P(t_1)\gamma_5 M_q^{-1}\gamma_5 P(t_0)^T\gamma_5\mathcal{W}\right]^\dagger \\
&= -\left[P(t_2)\gamma_5 M_q^{-1} P(t_1)^T \gamma_4 e^{-iq} P(t_1) V_{a1}\right]^\dagger \\
&= -\left[P(t_2)\gamma_5 V_{a3}^{(4,\mathrm{PC})}\right]^\dagger, \qquad (21)
\end{aligned}$$

where we have introduced a SST propagator called $a3$ (specialized to $\mu = 4$ here),

$$V_{a3}^{(\mu,\mathrm{PC})}(\boldsymbol{q}) \equiv M_q^{-1} P(t_1)^T [\gamma_\mu e^{-iq} P(t_1) V_{a1}]. \qquad (22)$$

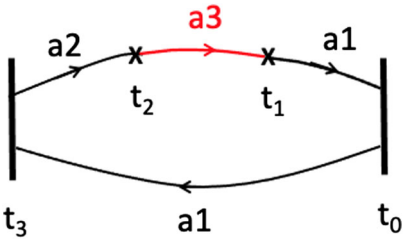

FIG. 3. Diagram (b) in terms of quark propagators: one part is V_{a1} to the pion wall at t_3, then V_{a2} to the current insertion at t_2; the other is a SST propagator V_{a3} (red) built from V_{a1} and the current insertion at t_1.

This expression indicates that $V_{a3}^{(4,\mathrm{PC})}$ can be obtained by a standard inversion $Mx = b$ with a "spatially extended source" $b = [\gamma_4 e^{-iq} P(t_1) V_{a1}]$ at t_1. This source is constructed from a previously defined quark propagator V_{a1} and the current insertion, hence the name "sequential source". Using $(a1, a2)$ and the newly defined propagator $a3$, the final expression for diagram (b) takes the form,

$$\begin{aligned}
\tilde{Q}_{44}^{(b,\mathrm{PC})}(\boldsymbol{q},t_2) = -\frac{5}{9} Z_V^2 \kappa^2 \mathrm{Tr}_{s,c}\Big[&[P(t_2)\gamma_5 V_{a3}^{(4,\mathrm{PC})}(\boldsymbol{q})]^\dagger \\
&\times \gamma_4 e^{-iq} P(t_2) V_{a2} \mathcal{W}^T P(t_3)\gamma_5 V_{a1}\Big]. \qquad (23)
\end{aligned}$$

Figure 3 is a schematic depiction of how the propagators form the full correlation function in Eq. (23).

For conserved current, there are eight terms contributing to diagram (b) in Eq. (B6). Following the same procedure as for point current, the final expression for diagram (b) from point-split current can be written as

$$\begin{aligned}
\tilde{Q}_{44}^{(b,\mathrm{PS})}(\boldsymbol{q},t_2) &= \frac{1}{9}\kappa^2(d_1 + d_3 + d_5 + d_7 + d_{25} + d_{31} + d_{37} + d_{43}) \\
&= -\frac{5}{9}\kappa^2 \mathrm{Tr}_{s,c}\Big[[P(t_2)\gamma_5 V_{a3}^{(4,\mathrm{PS})}(\mathbf{q})]^\dagger (1-\gamma_4) e^{-iq} U_4(t_2, t_2+1) P(t_2+1) V_{a2} \mathcal{W}^T P(t_3)\gamma_5 V_{a1} \\
&\quad - [P(t_2+1)\gamma_5 V_{a3}^{(4,\mathrm{PS})}(\mathbf{q})]^\dagger (1+\gamma_4) U_4^\dagger(t_2+1, t_2) e^{-iq} P(t_2) V_{a2} \mathcal{W}^T P(t_3)\gamma_5 V_{a1}\Big], \qquad (24)
\end{aligned}$$

where a new inversion is needed for the SST propagator,

$$\begin{aligned}
V_{a3}^{(4,\mathrm{PS})}(\boldsymbol{q}) \equiv M_q^{-1}\Big[&P^T(t_1)(1-\gamma_4) e^{-iq} U_4(t_1, t_1+1) \\
&\times P(t_1+1) V_{a1} - P^T(t_1+1)(1+\gamma_4) \\
&\times U_4^\dagger(t_1+1, t_1) e^{-iq} P(t_1) V_{a1}\Big]. \qquad (25)
\end{aligned}$$

This is the point-split version of Eq. (22) with $\mu = 4$. Since the current is split in the t direction, U_4 and $U_4^\dagger$ commute with e^{-iq} in these two equations.

3. Diagram (c) (same flavor Z-graph) and SST

For local current, there are two terms, d_0 and d_9 in Eq. (B4), that are contributing to the connected part of same-flavor correlations. They are characterized by the same charge factors $q_u q_u = 4/9$ or $q_{\bar{d}} q_{\bar{d}} = 1/9$. The d_0 diagram is a clockwise propagation $t_0 \to t_3 \to t_1 \to t_2 \to t_0$ where the two currents couple to the u quark, while the d_9 diagram is a counterclockwise propagation $t_0 \to t_2 \to t_1 \to t_3 \to t_0$ where the two currents couple to the d quark. They are essentially the Z-graph of diagram (b) with the

current insertions 1 and 2 switched, whose correlation function can be written as

$$\tilde{Q}_{44}^{(c,\mathrm{PC})} = \frac{5}{9} Z_V^2 \kappa^2 \mathrm{Tr}_{s,c}\Big[\gamma_5 \mathcal{W}^T S(t_0,t_2)\gamma_4 e^{-iq} S(t_2,t_1) \times \gamma_4 e^{iq} S(t_1,t_3)\mathcal{W}\mathcal{W}^T\gamma_5 S(t_3,t_0)\mathcal{W}\Big]. \quad (26)$$

First we isolate the $t_3 \to t_1 \to t_2$ propagation,

$$\begin{aligned} &S(t_2,t_1)\gamma_4 e^{iq} S(t_1,t_3)\mathcal{W} \\ &= P(t_2) M_q^{-1} P(t_1)^T \gamma_4 e^{iq} P(t_1) M_q^{-1} P(t_3)^T \mathcal{W} \\ &= P(t_2) M_q^{-1} P(t_1)^T \gamma_4 e^{iq} P(t_1) V_{a2} \equiv P(t_2) V_{a4}^{(4,\mathrm{PC})}(\boldsymbol{q}), \end{aligned} \quad (27)$$

where a new SST propagator is introduced (specialized to $\mu = 4$ here),

$$V_{a4}^{(\mu,\mathrm{PC})}(\boldsymbol{q}) \equiv M_q^{-1} P(t_1)^T [\gamma_\mu e^{iq} P(t_1) V_{a2}]. \quad (28)$$

Using $a1$ and $a4$, the final expression for diagram (c) using point current takes the form,

$$\tilde{Q}_{44}^{(c,\mathrm{PC})}(\boldsymbol{q},t_2) = \frac{5}{9} Z_V^2 \kappa^2 \mathrm{Tr}_{s,c}\Big[[\gamma_4 e^{iq} P(t_2)\gamma_5 V_{a1}]^\dagger P(t_2) \times V_{a4}^{(4,\mathrm{PC})}(\boldsymbol{q}) \mathcal{W}^T P(t_3)\gamma_5 V_{a1}\Big]. \quad (29)$$

Figure 4 is a schematic depiction of how the propagators form this correlation function.

For conserved current, there are eight terms contributing to diagram (c) in Eq. (B6). Following a similar procedure as for local current, the final expression for diagram (c) from point-split current can be written as

$$\begin{aligned} \tilde{Q}_{44}^{(c,\mathrm{PS})}(\boldsymbol{q},t_2) &= \frac{1}{9}\kappa^2(d_0 + d_2 + d_4 + d_6 + d_{27} + d_{33} + d_{39} + d_{45}) \\ &= \frac{5}{9}\kappa^2 \mathrm{Tr}_{s,c}\Big[[P(t_2)\gamma_5 V_{a1}]^\dagger (1-\gamma_4) e^{-i\mathbf{q}} U_4(t_2,t_2+1) P(t_2+1) V_{a4}^{(4,\mathrm{PS})}(\mathbf{q}) \mathcal{W}^T P(t_3)\gamma_5 V_{a1} \\ &\quad - [P(t_2+1)\gamma_5 V_{a1}]^\dagger (1+\gamma_4) U_4^\dagger(t_2+1,t_2) e^{-i\mathbf{q}} P(t_2) V_{a4}^{(4,\mathrm{PS})}(\mathbf{q}) \mathcal{W}^T P(t_3)\gamma_5 V_{a1}\Big], \end{aligned} \quad (30)$$

where

$$V_{a4}^{(4,\mathrm{PS})}(\boldsymbol{q}) \equiv M_q^{-1}\Big[P^T(t_1)(1-\gamma_4) e^{iq} U_4(t_1,t_1+1) P(t_1+1) V_{a2} - P(t_1+1)^T (1+\gamma_4) U_4^\dagger(t_1+1,t_1) e^{iq} P(t_1) V_{a2}\Big]. \quad (31)$$

Compare to Eq. (25) for diagram (b), this expression has $a2$ instead of $a1$, $\boldsymbol{q}$ instead of $-\boldsymbol{q}$.

The total connected contribution to the polarizabilities in Eq. (1) is simply the sum of the individual normalized terms in Fig. 2,

$$Q_{44}(\boldsymbol{q},t_2,t_1) = Q_{44}^{(a)} + Q_{44}^{(b)} + Q_{44}^{(c)}, \quad (32)$$

for either point current or conserved current. The charge factors and flavor-equivalent contributions have been included in each diagram.

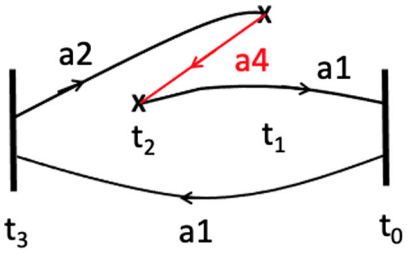

FIG. 4. Diagram (c) in terms of quark propagators; $a1$ from t_0 to t_3, SST quark propagator $a4$ (red) with sequential source built from $a2$ and current insertion at t_1, and $a1$ from t_2 to t_0. This is the Z-graph of diagram (b).

IV. SIMULATION DETAILS AND RESULTS

Having laid out the methodology and detailed the correlation functions, we now discuss how to numerically evaluate them in a Monte Carlo simulation in order to extract the polarizability. As a proof-of-principle test, we use quenched Wilson action with $\beta = 6.0$ and $\kappa = 0.1520$, 0.1543, 0.1555, 0.1565 on the lattice $24^3 \times 48$. The pion mass corresponding to the kappas will be determined in our simulation. We analyzed 1000 configurations for each of the kappas. The scale of this action has been determined in Ref. [55], with inverse lattice spacing $1/a = 2.312$ GeV and kappa critical $\kappa_c = 0.15708$. It also gives the pion mass as a function of kappa,

$$(m_\pi a)^2 = 2.09 \times \frac{1}{2}\left(\frac{1}{\kappa} - \frac{1}{\kappa_c}\right), \quad (33)$$

which will be compared with the measured m_π. Dirichlet (or open) boundary condition is imposed in the time direction, while periodic boundary conditions are used in spatial dimensions. The pion source is placed at $t_0 = 7$ and sink at $t_3 = 42$ (time is labeled from 1 to 48). One current is inserted at a fixed time t_1, while the other current t_2 is free

to vary. We use integers $\{n_x, n_y, n_z\}$ to label the discrete momentum on the lattice,

$$\boldsymbol{q} = \left\{\frac{2\pi n_x}{L_x}, \frac{2\pi n_y}{L_y}, \frac{2\pi n_z}{L_z}\right\}, \quad n_x, n_y, n_z = 0, \pm 1, \pm 2, \ldots, \tag{34}$$

and consider five different combinations $\{0,0,0\}$, $\{0,0,1\}$, $\{0,1,1\}$, $\{1,1,1\}$, $\{0,0,2\}$. In lattice units they correspond to the values $\boldsymbol{q}^2 a^2 = 0$, 0.068, 0.137, 0.206, 0.274, or in physical units to $\boldsymbol{q}^2 = 0$, 0.366, 0.733, 1.100, 1.465 (GeV^2). In order to evaluate the connected diagrams, we need four inversions of the quark matrix with varying sources; two wall-sourced propagators V_{a1} and V_{a2}, and two SST propagators $V_{a3}^{(4,\mathrm{PS})}(\boldsymbol{q})$ and $V_{a4}^{(4,\mathrm{PS})}(\boldsymbol{q})$ at a fixed $\boldsymbol{q}$. So the count for five momenta is $2 + 2 \times 5 = 12$ per kappa per configuration. It takes longer to do the inversions for larger kappas due to critical slowing down.

A. Raw correlation functions

First, we discuss how to determine pion mass from the various two-point functions in Sec. III A. In Fig. 5 we show the wall-to-wall pion correlations based on Eq. (12) (Type 1) and Eq. (13) (Type 2) at $\kappa = 0.1555$. Type 1 only depends on the $a1$ quark propagator originating from the wall source at $t_0 = 7$. Instead of ending at fixed $t_3 = 42$, we allow it to vary in the entire range of t on the lattice. One can visualize it as a moving wall sink. In this way, we get to observe a plateau in the effective mass function which we use to extract the mass. Similarly, Type 2 only depends on the $a2$ quark propagator originating from the wall source at $t_3 = 42$. Instead of ending at fixed $t_0 = 7$, we allow it to vary in the entire range of t on the lattice. We flip the sign of its effective mass function so a direct comparison of the plateaus for the two types can be made. We use Type 1 with a varying sink to extract pion and rho masses at the four kappa values. We obtain approximately 1100, 800, 600, and 370 MeV for pion mass at $\kappa = 0.1520$, 0.1543, 0.1555, 0.1565, respectively. These values agree well with those predicted from the relation in Eq. (33). From this point on, we will refer to pion mass rather than kappa values. The rho meson is considered in this work to judge the efficacy of vector meson dominance in charge radius extraction. More precise numbers for m_π and m_ρ with uncertainties will be given in the summary table at the end (Table I). Another benefit of plotting the Type 1 and Type 2 correlators with a varying sink is we get to see the limited "window of opportunity" in the effective mass where ground state dominates. This is the window in which we study the current-current correlations. We utilize this information to fix one of the two currents in the four-point function calculation so it mainly couple to the zero-momentum ground state. Having examined the plots, we settle on

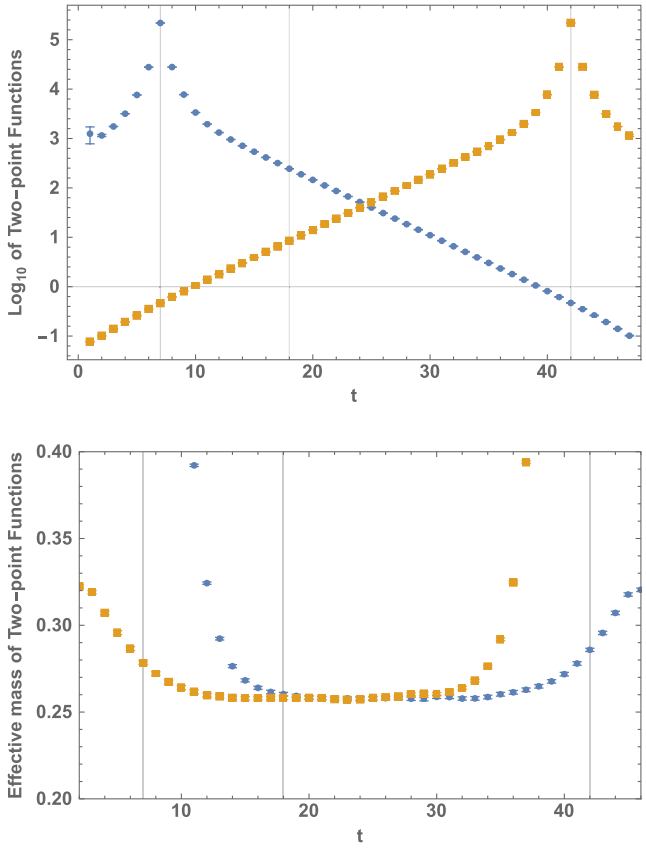

FIG. 5. Moving sink zero-momentum pion correlator Type 1 (blue) and Type 2 (orange) and their effective mass functions at $m_\pi = 600$ MeV. They are constructed from either $a1$ or $a2$ quark propagators as explained in the text. The vertical gridlines indicate the three fixed-time points in the study. These functions can be used to extract the pion mass in single-exponential fashion. The value at $t_3 = 42$ in Type 1 or at $t_0 = 7$ in Type 2 can be used for normalization of four-point functions.

$t_1 = 18$, 18, 18, 14 for $m_\pi = 1100$, 800, 600, 370 MeV, respectively.

Next, we discuss normalization constant for four-point functions. This is the zero-momentum wall-to-wall two-point function in the denominator of Eq. (4). We have three options, corresponding to the three types in Eqs. (12)–(14). Type 1 normalization constant is simply the special value at $t = t_3 = 42$ in the blue curve of Fig. 5, and Type 2 the special value at $t = t_0 = 7$ in the orange curve of Fig. 5. Type 3 normalization constant is computed separately. The three types are not expected to agree configuration by configuration since they originate from different wall sources, but they should approach the same value in the configuration average within statistics. We found the numerical values 0.4683(6), 0.4672(6), 0.468(7), from Type1, Type2, and Type 3, respectively, at this pion mass. We see that Type 3 has larger statistical uncertainties than in Type 1 and Type 2. This is expected since Type 3 is constructed from two wall sources, while the other two from

TABLE I. Summary of results in physical units from two-point and four-point functions. Charge radius is chirally extrapolated to the physical point, as well as α_E elastic and α_E total. The α_E inelastic at the physical point is taken as the difference of the two. Known values from ChPT and PDG are listed for comparison purposes. All polarizabilities are in units of 10^{-4} fm^3.

	$\kappa = 0.1520$	$\kappa = 0.1543$	$\kappa = 0.1555$	$\kappa = 0.1565$	Physical point	Known value
m_π (MeV)	1104.7 ± 1.2	795.0 ± 1.1	596.8 ± 1.4	367.7 ± 2.2	138	138
m_ρ (MeV)	1273.1 ± 2.5	1047.3 ± 3.4	$930. \pm 7$	$830. \pm 17$	770	770
$\langle r_E^2 \rangle$ (fm^2)	0.1424 ± 0.0029	0.195 ± 0.007	0.257 ± 0.005	0.304 ± 0.016	0.40 ± 0.05	0.434 ± 0.005 (PDG)
α_E elastic	0.618 ± 0.012	1.17 ± 0.04	2.07 ± 0.04	3.97 ± 0.21	13.9 ± 1.8	15.08 ± 0.13 (PDG)
α_E inelastic	-0.299 ± 0.019	-0.672 ± 0.030	-0.92 ± 0.11	-1.27 ± 0.13	-9.7 ± 1.9 to -5.1 ± 2.0	
α_E total	0.319 ± 0.023	0.50 ± 0.05	1.15 ± 0.11	2.70 ± 0.25	4.2 ± 0.5 to 8.8 ± 0.9	2.93 ± 0.05 (ChPT) $2.0 \pm 0.6 \pm 0.7$ (PDG)

one. We will use Type 3 as normalization for the reason to be discussed below.

Having determined the two-point functions, we present in Fig. 6 the raw normalized four-point functions Q_{44} at five different values of momentum $\boldsymbol{q}$ and at $m_\pi = 600$ MeV. For comparison purposes, all points in Q_{44} are displayed on the same linear scale. For the effective mass function $\ln Q_{44}(t)/Q_{44}(t+1)$, only points between the pion walls are displayed for clarity. The results are based on conserved currents and only the connected diagrams (a), (b), and (c). There are a number of interesting features in these plots.

First, the results for $\boldsymbol{q} = 0$ confirms the current conservation property discussed in Eq. (A9). Basically, for conserved current, we expect the ratio of four-point function to two-point function to approach the charge factor $2q_u q_{\bar{d}} = 4/9$ for diagram (a) in the isospin limit,

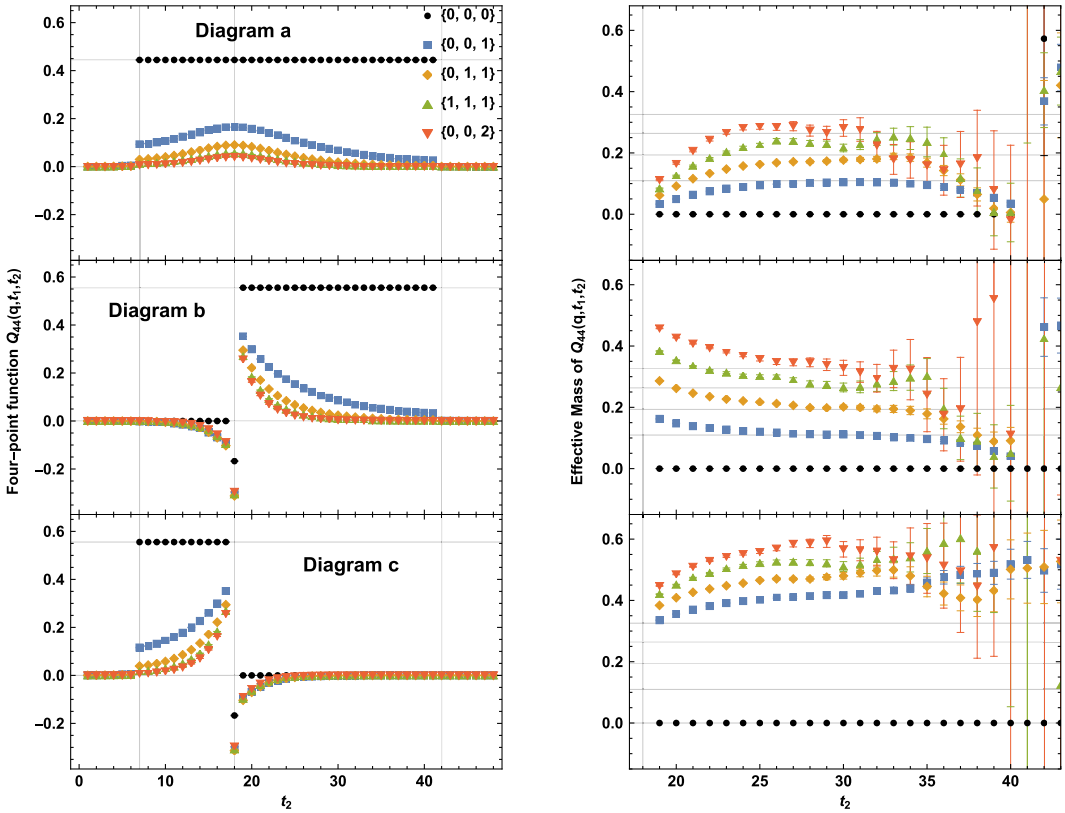

FIG. 6. Normalized four-point functions (left panel) and their effective mass functions (right panel) from the connected diagrams as a function of current separation at $m_\pi = 600$ MeV. The $\boldsymbol{q} = 0$ results serve as a check of current conservation. The results for nonzero $\boldsymbol{q}$ between $t_2 = 18$ and $t_2 = 41$ will become the basis for our analysis. The vertical gridlines indicate the pion walls ($t_0 = 7$ and $t_3 = 42$) and the fixed current insertion ($t_1 = 18$). The horizontal gridlines in the effective mass functions indicate the value of $E_\pi - m_\pi$ where the continuum dispersion relation $E_\pi = \sqrt{\boldsymbol{q}^2 + m_\pi^2}$ is used.

independent of current insertion points t_1 and t_2. For diagrams (b) and (c), the factor is $q_u q_u + q_{\bar{d}} q_{\bar{d}} = 5/9$. Indeed, this is confirmed in all three diagrams (black dots). In diagram (a), current conservation is limited between $t_2 = 7$ (on the pion-wall source) and $t_2 = 41$ (one step inside the pion-wall sink) because the two currents independently couple to two different quarks in this range. In diagram (b), where they couple to the same quark, current conservation emerges only starting from $t_2 = 19$. In diagram (c), it is limited between $t_2 = 7$ and $t_2 = 17$ because it is the Z-graph of (b) (different time ordering). If diagrams (b) and (c) are added, then current conservation extends to the whole range, just like diagram (a), except for the special point of $t_1 = t_2$ to be discussed below. Outside the regions of current conservation, the $\boldsymbol{q} = 0$ signal is exactly zero, while the $\boldsymbol{q} \neq 0$ signal gradually goes to zero towards the Dirichlet wall.

Second, we found that although we have three options for two-point functions to be used as normalization, they have different statistical fluctuations. This is demonstrated in Fig. 7 where we plot the three types for a select few configurations out of the 1000, using diagram (a) at zero momentum and a fixed time slice in the conserved region ($7 < t_2 < 41$) as an example. For each type, we plot separately the unnormalized four-point function, two-point function, and their ratios. We see that the ratio from Type 3 gives the expected value (4/9) exactly whereas Type 1 and Type 2 fluctuate around it. The reason is that Type 3, despite being more noisy than Type 1 and Type 2, is exactly correlated with the four-point function configuration by configuration, both being constructed from the same two wall sources. We rely on this perfect correlation in Type 3 to serve as a strong numerical validation that the wall sources and the conserved currents are correctly implemented in our study. At nonzero momentum ($\boldsymbol{q} \neq 0$), however, we found that all three normalization types produce comparable statistical uncertainties for the normalized four-point functions. Fig. 6 is plotted using Type 3 normalization.

Third, the special point of $t_1 = t_2$ is regular in diagram (a), but gives irregular results in diagram (b) and (c) for all values of $\boldsymbol{q}$. This is the contact term in the discussion surrounding Eq. (A9). We avoid this point in our analysis.

Fourth, we observe that the results about $t_1 = 18$ in diagrams (b) and (c) are mirror images of each other, simply due to the fact that they are from the two different time orderings of the same diagram. In principle, this property could be exploited to reduce the cost of simulations. In this study, however, we computed all three diagrams separately, and add them between $t_1 = 19$ and $t_3 = 41$ as the signal. We also note in passing that the Q_{44} signal in diagram (c) is negative definite whereas it is positive definite in diagrams (a) and (b).

Finally, the effective mass function of Q_{44} for diagram (b) approaches the value of $E_\pi - m_\pi$ at large separation

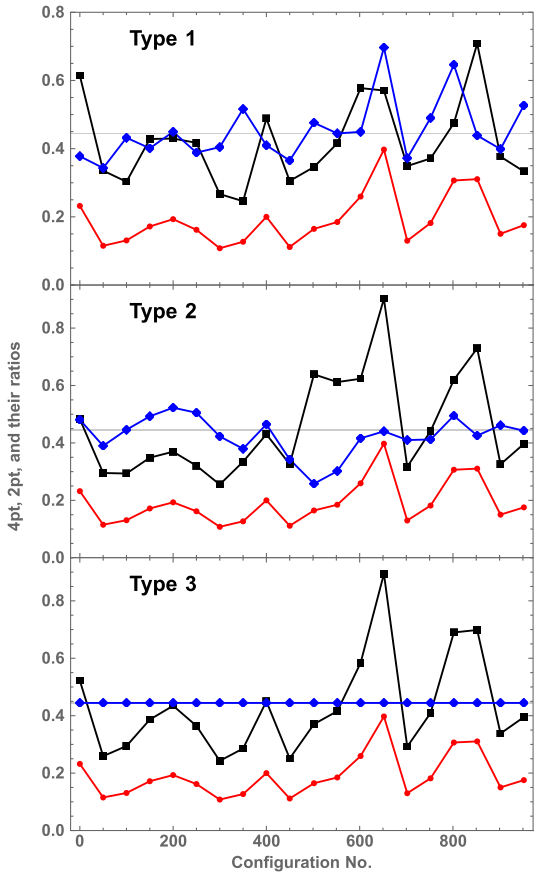

FIG. 7. Statistical fluctuations are shown in the unnormalized four-point function (red), three types of two-point functions (black), and their ratios (blue) at 20 randomly selected configurations. For this figure, diagram (a) at $\boldsymbol{q} = 0$ and $m_\pi = 600$ MeV is used as an example. Neighboring points are connected by straight lines to facilitate visualization. The faint horizontal gridline indicates the expected ratio 4/9 for this diagram and conserved currents.

times between t_1 and t_2. This is an indication that the four-point function for diagram (b) is dominated by the elastic contribution with a falloff rate of $E_\pi - m_\pi$ according to Eq. (7). The same is true for diagram (a), although deviations are slightly larger at higher momentum. The situation for diagram (c), however, is completely different. The falloff rates approach high above their respective $E_\pi - m_\pi$ values, suggesting they are dominated by inelastic contributions. In other words, the intermediate state is not a pion, but some four-quark state at higher mass and energy.

We also used local current as a guide to develop our formalism and algorithms. If we take four-point function ratio at zero momentum, we expect $\tilde{Q}_{44}^{(\mathrm{PS})}(\boldsymbol{0})/\tilde{Q}_{44}^{(\mathrm{PC})}(\boldsymbol{0}) \to Z_V^2$ where $\tilde{Q}_{44}^{(\mathrm{PC})}$ is computed without the Z_V factor in the formulas. For example, we obtain an estimate of $Z_V \approx 1.35$ at $m_\pi = 600$ MeV, which is consistent with literature [56]. Since our results are based exclusively on conserved current, we will not discuss local current further.

B. Elastic form factor

The formula for electric polarizability in Eq. (1) involves the charge radius r_E and the elastic contribution Q_{44}^{elas}, both of which can be extracted from the large-time behavior of four-point functions Q_{44}. According to Eq. (8), Q_{44}^{elas} is expected to exhibit single-exponential behavior with a falloff rate of $E_\pi - m_\pi$. The form factor F_π is contained in the amplitude of this falloff. Based on the discussion about Fig. 6, diagrams (a) and (b) have the expected falloff whereas diagram (c) does not. As far as elastic contribution is concerned, we can drop diagram (c) and focus only on diagrams (a) and (b). This improves the form factor analysis by eliminating the inelastic 'contamination' from diagram (c). It can be regarded as a form of optimization in the analysis. Figure 8 shows an example of the four-point functions Q_{44}^{ab} including only diagrams (a) and (b), along with their effective mass functions. We focus in the region of signal between t_1 and t_3 and plot them as a function of time separation $t = t_2 - t_1$ between the two currents. Note that we exclude the $t = 0$ point from the analysis due to contact terms, as discussed earlier. We see that there is a region where the effective mass functions coincide with the $E_\pi - m_\pi$ gridlines, indicating that Q_{44}^{ab} is dominated by elastic contributions. The agreement is better at smaller momentum values. The signal at large times is noisy and increasingly so at higher momentum. We also see the effect of the Dirichlet wall which forces the effective mass to curve down. In this context, the inclusion of diagram (c) would push the elastic limit into larger times where the signal is lost. To account for possible violation of the continuum dispersion relation, we perform a fit to the functional form of Q_{44}^{elas} in Eq. (8), treating both $\{F_\pi, E_\pi\}$ as free parameters with m_π fixed at the measured values from two-point functions. Details of the fits at all four pion masses are given in Table II in Appendix D. From this table, we observe that the E_π from the fit largely agrees with that from the continuum dispersion relation. Deviations become more apparent at higher momentum.

After the form factor data are obtained, we fit them to the monopole form,

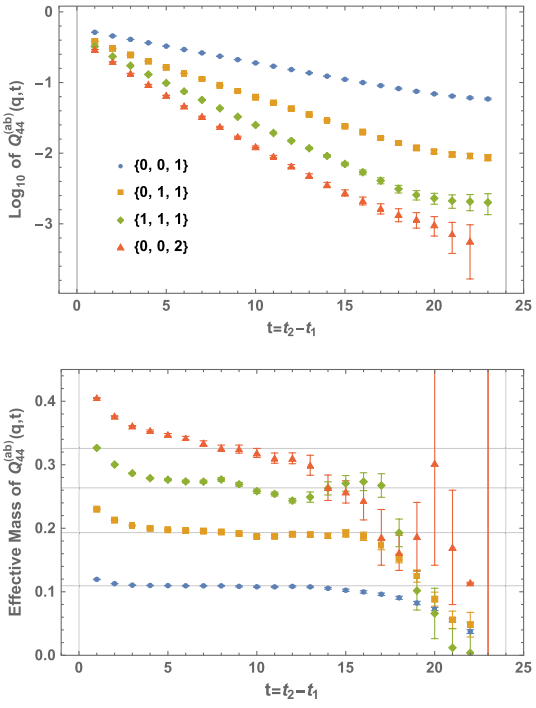

FIG. 8. Normalized four-point functions from diagrams (a) and (b) in log plot and their effective mass functions at different values of $\boldsymbol{q}$ and $m_\pi = 600$ MeV. They are plotted as functions of time separation $t = t_2 - t_1$ between the two currents relative to fixed $t_1 = 18$. The horizontal gridlines in the effective mass are $E_\pi - m_\pi$ using continuum dispersion relation for E_π with measured m_π. These functions are used to extract the elastic contributions Q_{44}^{elas}.

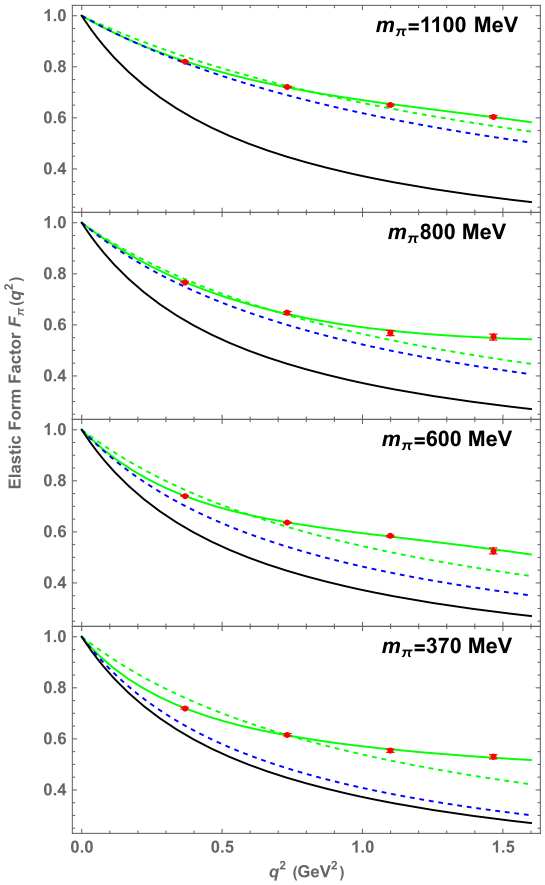

FIG. 9. Pion elastic form factors extracted from four-point functions. The red data points are the measured values in Table II. The green solid line is a fit to the z-expansion in Eq. (36). The green dashed line is a fit to the monopole form in Eq. (35). The blue dashed line is the same monopole form plotted with the measured rho mass, and the black solid line with the physical rho mass.

$$F_\pi(\boldsymbol{q}^2) = \frac{1}{1+\boldsymbol{q}^2/m_V^2}, \tag{35}$$

which is the well-known vector meson dominance (VMD) commonly considered in pion form factor studies. The results are illustrated in Fig. 9. We see that the monopole form does not fit the data well, especially at higher-momentum and lower-pion mass. We will not consider the monopole fit further. Instead, we opt for the z-expansion parametrization [57]

$$\begin{aligned} F_\pi(\boldsymbol{q}^2) &= 1 + \sum_{k=1}^{k_{\max}} a_k z^k, \\ \text{where } z &\equiv \frac{\sqrt{t_{\text{cut}} - t} - \sqrt{t_{\text{cut}} - t_0}}{\sqrt{t_{\text{cut}} - t} + \sqrt{t_{\text{cut}} - t_0}} \\ \text{and} \quad t &= -\boldsymbol{q}^2, \quad t_{\text{cut}} = 4m_\pi^2, \end{aligned} \tag{36}$$

where a_k are free parameters and t_{cut} is the two-pion production threshold. We take $t_0 = 0$ so the form goes through $F_\pi(0) = 1$ by construction. Using this form, we can find a good fit with $k_{\max} = 3$ in all cases. For comparison, we also plot the monopole function with the measured rho mass m_ρ and the physical rho mass of $m_\rho^{\text{phys}} = 0.77$ GeV. We observe significant differences between the fitted monopole form (m_V) and the VMD form (m_ρ). The difference grows with increasing momentum and decreasing pion mass. Similar behavior has been observed in previous studies [53,58]. This issue of form factors in the four-point function formalism deserves further study with more advanced setups, such as dynamical ensembles, smaller pion masses, and wider momentum coverage. Once the functional form of form factor is determined, the charge radius is obtained by

$$\langle r_E^2 \rangle = -6 \frac{dF_\pi(\boldsymbol{q}^2)}{d\boldsymbol{q}^2}\bigg|_{\boldsymbol{q}^2 \to 0}. \tag{37}$$

From the extracted charge radius, we attempt a chiral extrapolation using a quadratic form $a + bm_\pi + cm_\pi^2$. We also perform a chiral extrapolation of the elastic part of α_E using the form $\frac{a}{m_\pi} + b + cm_\pi$. The result is shown in Fig. 10. The extrapolated charge radius at the physics point is consistent with PDG value albeit our results suffer from relatively large statistical errors. The same is true for the elastic part of α_E in Eq. (1). Their values in physical units can be found in Table I.

C. Electric polarizability

Having obtained the elastic contribution Q_{44}^{elas}, we now turn to the inelastic part of α_E from Eq. (1). In Fig. 11 we show separately the total contribution Q_{44} (from all three diagrams) and Q_{44}^{elas} as a function of current separation

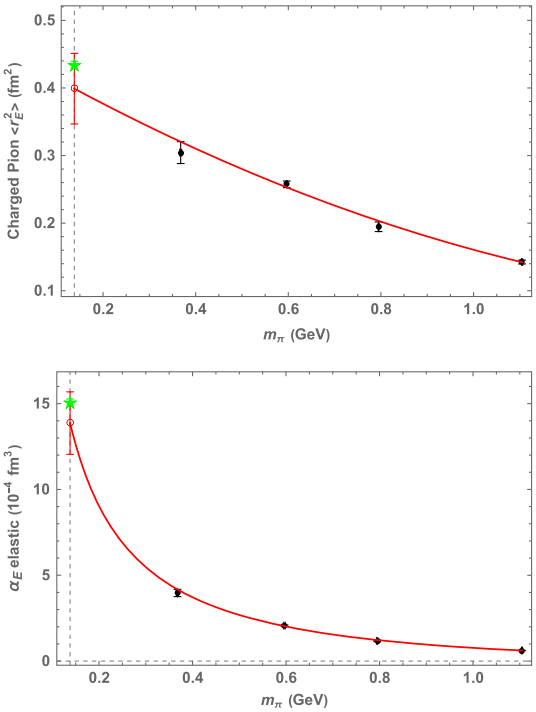

FIG. 10. Chiral extrapolation of charge radius (top) and the elastic part of electric polarizability (bottom). The green stars are derived from PDG values.

$t = t_2 - t_1$. We use $m_\pi = 600$ MeV as an example; the graphs at the other pion masses look similar. Note that although Q_{44}^{elas} is obtained in the large-time region, the subtraction is done in the whole region according to the functional form in Eq. (8). Most of the contribution is in the small time region where inelastic contributions are significant. We observe that Q_{44}^{elas} is consistently larger than Q_{44}, suggesting that the inelastic term in the formula is negative. The time integral is simply the negative of the shaded area between the two curves. One detail to notice is that the curves include the $t = 0$ point which has unphysical contributions in Q_{44} as mentioned earlier. We would normally avoid this point and only start the integral from $t = 1$. However, as one can see, the chunk of area between $t = 0$ and $t = 1$ is the largest piece in the integral. To include this contribution, we linearly extrapolated the Q_{44} term back to $t = 0$ using the two points at $t = 1$ and $t = 2$. This will incur a systematic effect on the order of $O(a^2)$ since the error itself is order of $O(a)$. As the continuum limit is approached, the systematic effect will vanish (the chunk will shrink to zero). There is no issue to include this point in Q_{44}^{elas} using its functional form.

The inelastic term can now be constructed by multiplying $2\alpha/\boldsymbol{q}^2$ and the time integral, and the whole term is a function of momentum. Since α_E is a static property, we extrapolate it to $\boldsymbol{q}^2 = 0$ smoothly. We consider three fits, a quadratic fit $a + bx + cx^2$ ($x = \boldsymbol{q}^2$) using all four data points, the same quadratic fit using the lowest three points,

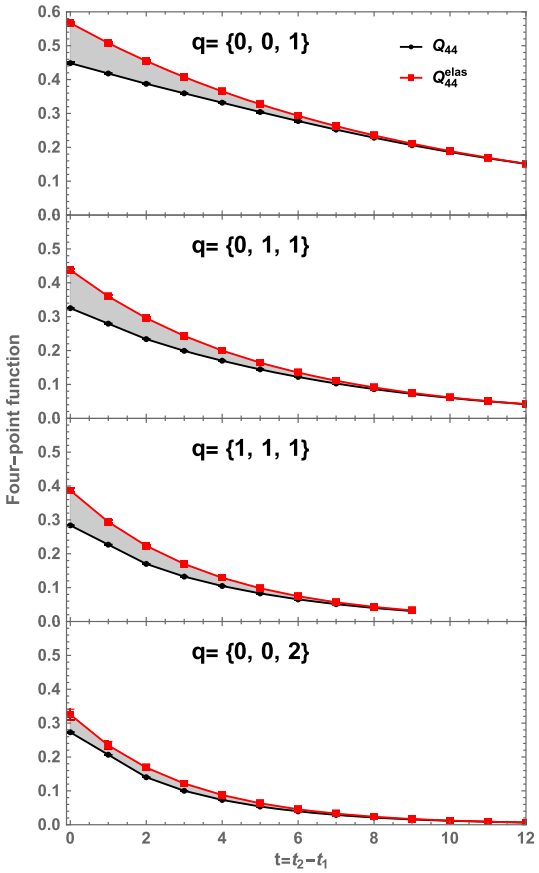

FIG. 11. Total Q_{44} and elastic Q_{44}^{elas} at different values of $\boldsymbol{q}$ at $m_\pi = 600$ MeV. The shaded area, $(1/a)\int dt[Q_{44}(\boldsymbol{q},t) - Q_{44}^{\text{elas}}(\boldsymbol{q},t)]$, is the dimensionless signal contributing to polarizability.

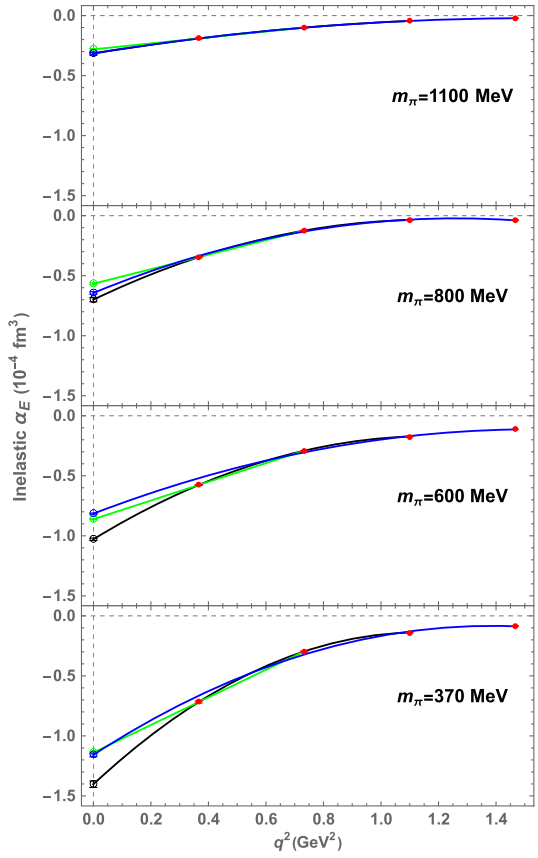

FIG. 12. Momentum dependence of the inelastic term in Eq. (1) and its extrapolation to $\boldsymbol{q}^2 = 0$ at all pion masses. Red points are based on the shaded areas in Fig. 11. Blue curve is a quadratic extrapolation using all points. Black curve is the same quadratic extrapolation using the three lowest points. Green curve is a linear extrapolation based on the two lowest points. Empty points indicate the corresponding extrapolated values contributing to α_E.

and a linear fit using the two lowest points. The results are shown in Fig. 12 for all pion masses. One observes a spread in the extrapolated values. The fits with four or two points do not capture the curvature in the data; only the one with three points does. We treat the spread as a systematic effect as follows. We take the average of the largest spread out of the three values at each pion mass, and it comes with a statistical uncertainty. We then take half value of the spread as a systematic uncertainty. The statistical and systematic uncertainties are then propagated in quadrature to the analysis of α_E. For our data, the statistical uncertainties are relatively small, so the systematic uncertainties from the extrapolation are dominant in the inelastic contribution.

Finally, we assemble the two terms in the formula in Eq. (1) to obtain α_E in physical units. To see how the trend continues to smaller pion masses, we take the total values for α_E at the four pion masses and perform a smooth extrapolation to the physical point. Since our pion masses are relatively large, we consider two forms to cover the range of uncertainties in the extrapolation: a polynomial form $a + bm_\pi + cm_\pi^3$ and a form $\frac{a}{m_\pi} + bm_\pi + cm_\pi^3$ inspired by ChPT [59]. The spread can be considered as a systematic effect. Since ChPT for pions has no m_π^2 term, we choose to leave it out in the forms. The leading $1/m_\pi$ term is divergent at the chiral limit. The extrapolated value of 4.2 ± 0.5 to 8.8 ± 0.9 is higher than the known value from ChPT at two loop [47] which gives $\alpha_E = 2.93(5)$, and from PDG [60] which quotes a value $\alpha_E = 2.0(6)(7)$ from experiment with large uncertainties. Combining the chirally extrapolated total and the previously chirally extrapolated elastic term from Fig. 10, we obtain the inelastic term by taking the difference of the two. This yields a prediction of -9.7 ± 1.9 to -5.1 ± 2.0 for the inelastic value at the physics point. We should mention that the range is slightly smaller in magnitude than the inelastic contribution obtained in another lattice study [36] near physical pion mass. It employs a formula derived from a different method but has a similar structure.

We summarize the results in Fig. 13 and in Table I. At the pion masses explored, our lattice results show a clear pattern for electric polarizability: the elastic term makes a positive

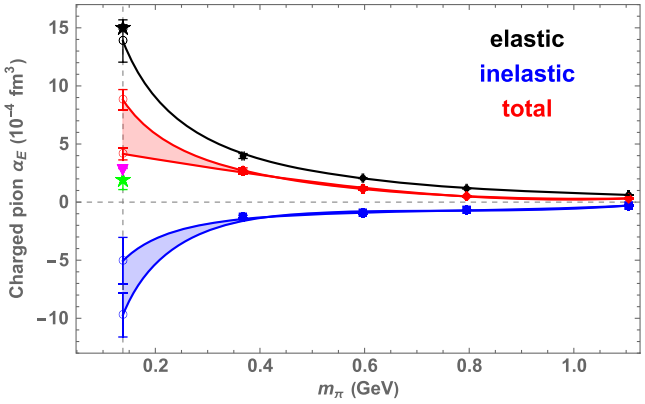

FIG. 13. Pion mass dependence of electric polarizability of a charged pion from four-point functions in lattice QCD. Elastic and inelastic contributions correspond to the two terms in the formula in Eq. (1). Elastic and total are chirally extrapolated to the physical point. Inelastic is the difference of the two. Empty circles are extrapolated values at the physical point. Magenta triangle is known value from ChPT. Black and green stars are PDG values for elastic and total, respectively.

contribution, whereas the inelastic term makes a negative and smaller in magnitude contribution. The cancellation leads to a positive value in the total. The cancellation appears to continue in the approach to the physical point, but it is less conclusive quantitatively, as indicated by the uncertainty bands from extrapolations. This points to the importance of exploring smaller pion masses in future simulations.

V. SUMMARY AND OUTLOOK

We investigated the feasibility of using four-point functions in lattice QCD to extract charged pion electric polarizability. The approach is based on low-energy Compton scattering tensor constructed with quark and gluon fields in Euclidean spacetime [38]. The central object is the formula given in Eq. (1) which consists of two terms. One is an elastic contribution involving charge radius $\langle r_E^2 \rangle$ and pion mass. The other an inelastic contribution in the form of a subtracted time integral. In addition to four-point functions, it requires two-point functions for pion mass and normalization, but not three-point functions. The elastic contribution can be obtained from the same four-point function in the elastic limit.

We laid out a detailed formalism and notation using standard Wilson fermion as a baseline. Although we use both local current and conserved current on the lattice to develop and test the formalism, our results are based on conserved current on the lattice. It sidesteps the renormalization issue ($Z_V = 1$), but comes with increased complexity in implementation. To apply the special kinematics (zero-momentum Breit frame) in the formula, we employ wall sources without gauge-fixing for the creation and annihilation of pions. We show how to construct the four-point functions using SST quark propagation, develop efficient algorithms for numerical evaluation, and use a high-performance solver [61].

We carried out a proof-of-concept simulation using quenched Wilson action with pion mass ranging from 1100 MeV to 370 MeV. We only considered the connected contributions in this work. We discussed three types of wall-to-wall two-point functions for normalization. We found a perfect correlation between the four-point function $Q_{44}(\boldsymbol{q}^2 = 0)$ and Type 3 two-point function imposed by current conservation, configuration by configuration. This property provides a strong check of our implementation.

The analysis procedure used to determine α_E in Eq. (1) involves multiple steps which we summarize here: 1) Fit Type 1 two-point function to obtain m_π (and m_ρ). 2) Fit four-point function $Q_{44}^{(ab)}$ from diagrams (a) and (b) to Q_{44}^{elas} at large times for elastic form factor F_π. 3) Fit F_π data to a functional form, then extract charge radius $\langle r_E^2 \rangle$ which is then chirally extrapolated. 4) Perform subtraction $Q_{44}^{(abc)}(\boldsymbol{q}) - Q_{44}^{\text{elas}}(\boldsymbol{q})$ at small times using all three diagrams (a), (b), and (c). Do the time integration. Extrapolate back to $t = 0$ to include the missing chunk due to contact terms. 5) Extrapolate the inelastic term to $\boldsymbol{q}^2 = 0$ to obtain the static limit, then assemble everything in physical units for α_E. 6) Extrapolate the elastic and total α_E in pion mass to the physical point, obtain the inelastic by taking the difference.

Our results at the pion masses explored so far reveal a clear physical picture for charged pion α_E; it is the result of a cancellation between a positive elastic contribution and a negative inelastic contribution. It would be interesting to see how the cancellation plays out in the approach to the physical point. Nevertheless, the simulation demonstrates that the four-point function methodology can be a viable alternative to the background method for polarizabilities of charged hadrons. We caution that the picture is subject to a number of systematic effects not incorporated at this stage, such as the quenched approximation, finite-volume effects, and disconnected loops. Other sources of uncertainty in the present analysis include fitting the elastic form factor, the contact term at $t = 0$ in the inelastic term, and the extrapolation of the inelastic term to $\boldsymbol{q}^2 = 0$. All these open issues deserve further study in future simulations.

Going forward, the investigation can proceed in multiple directions. First, the quenched approximation should be removed by employing dynamical fermions. Work is underway to use our collection of two-flavor nHYP-clover ensembles [62] which have been successfully used in a number of physics projects. They have smaller pion masses (about 315 MeV and 227 MeV) that can be used to check the expected chiral behavior and facilitate a chiral extrapolation study. The elongated geometries in these ensembles offer a cost-effective way of studying finite-volume effects and reaching smaller $\boldsymbol{q}$ values. It would be interesting to see

how the charge radius is affected by the change of action. Second, a simulation of charged pion magnetic polarizability (β_M) is straightforward. The formula has been derived in Ref. [38]. One just needs to replace Q_{44} with Q_{11} in the formalism. It would be interesting to check the well-known prediction $\alpha_E + \beta_M \approx 0$ from ChPT. Third, the disconnected contributions should be included. This is a challenging task. Although disconnected loops generally give smaller contributions than connected ones, they must be dealt with for a complete picture from lattice QCD. Fourth, the methodology can be equally applied to neutral particles (for example π^0 and the neutron). The advantage it offers over the background field method is the natural treatment of disconnected loops (or sea quarks) [4,5]. Our ultimate target is the proton for which a formula is also available [38]. A first-principles-based calculation of its polarizabilities will be a valuable addition to the Compton scattering effort in nuclear physics.

ACKNOWLEDGMENTS

This work was supported in part by U.S. Department of Energy under Grant No. DE-FG02-95ER40907 (F. L., A. A.) and UK Research and Innovation Grant MR/S015418/1 (C. C.). A. A. would like to acknowledge support from University of Maryland. W. W. would like to acknowledge support from the Baylor College of Arts and Sciences Summer Research Award (SRA) program.

APPENDIX A: OPERATORS AND CURRENT CONSERVATION

To evaluate Eq. (4) in lattice QCD, we use standard annihilation (ψ) and creation ($\psi^\dagger$) operators for a charged pion,

$$\psi_{\pi^+}(x) = \bar{d}(x)\gamma_5 u(x), \qquad \psi^\dagger_{\pi^+}(x) = -\bar{u}(x)\gamma_5 d(x). \quad \text{(A1)}$$

We also consider rho meson two-point functions constructed from,

$$\psi_\rho(x)_i = \bar{d}(x)\gamma_i u(x), \quad i = 1,2,3, \quad \text{(A2)}$$

and average over the spatial directions. For Wilson fermions, the Dirac operator $M_q = \not{D} + m_q$ takes the standard form for a single-quark flavor labeled by q,

$$M_q = \mathbb{1} - \kappa_q \sum_\mu \left[(1-\gamma_\mu)U_\mu + (1+\gamma_\mu)U^\dagger_\mu\right], \quad \text{(A3)}$$

where $\kappa_q = 1/(2m_q + 4)$ is the hopping parameter and m_q the bare quark mass.

For current operators, we consider two options. One is the lattice local (or point) current built from up and down quark fields,

$$j^{(\mathrm{PC})}_\mu \equiv Z_V \kappa (q_u \bar{u}\gamma_\mu u + q_d \bar{d}\gamma_\mu d). \quad \text{(A4)}$$

The factor κ here is to account for the quark-field rescaling $\psi \to \sqrt{2\kappa}\psi$ in Wilson fermions. The factor 2 is canceled by the $1/2$ factor in the definition of the vector current $\frac{1}{2}\bar{\psi}\gamma_\mu\psi$. The charge factors are $q_u = 2/3$ and $q_d = -1/3$ where the resulting $e^2 = \alpha \approx 1/137$ in the four-point function has been absorbed in the definition of α^π_E. The advantage of this operator is that it leads to simple correlation functions. The drawback is that the renormalization constant for the vector current (Z_V) has to be determined.

We also consider conserved vector current on the lattice ($Z_V \equiv 1$) which can be derived by the Noether procedure. For the Wilson fermion action $S = \bar{\psi}_q M_q \psi_q$ built from the matrix in Eq. (A3), the simplest way [63] is to substitute the gauge fields by

$$U_\mu(x) \to U_\mu(x) e^{i q_q v^q_\mu}, \quad \text{(A5)}$$

and differentiate with respect to the external vector field v^q_μ, then take $v^q_\mu \to 0$. The result is the point-split form

$$\begin{aligned} j^{(q,\mathrm{PS})}_\mu(x) &= -i \left.\frac{\delta S}{\delta v^q_\mu}\right|_{v^q_\mu \to 0} \\ &= -q_q \kappa_q \Big[\bar{\psi}_q(x)(1-\gamma_\mu)U_\mu(x)\psi_q(x+\hat{\mu}) \\ &\quad - \bar{\psi}_q(x+\hat{\mu})(1+\gamma_\mu)U^\dagger_\mu(x)\psi_q(x)\Big]. \end{aligned} \quad \text{(A6)}$$

The phase factor $-i$ is explained in Ref. [64]. An alternative method [65,66] is through a local transformation on the quark fields, $\psi \to e^{-i\omega(x)}\psi$, and do variation $\frac{\delta S}{\delta(\Delta_\mu \omega)}$ on the finite difference $\Delta_\mu \omega = \omega(x+\hat{\mu}) - \omega(x)$. For two-quark flavors (u and d), we have

$$\begin{aligned} j^{(\mathrm{PS})}_\mu(x) &= q_u \kappa_u \Big[-\bar{u}(x)(1-\gamma_\mu)U_\mu(x)u(x+\hat{\mu}) \\ &\quad + \bar{u}(x+\hat{\mu})(1+\gamma_\mu)U^\dagger_\mu(x)u(x)\Big] \\ &\quad + q_d \kappa_d \Big[-\bar{d}(x)(1-\gamma_\mu)U_\mu(x)d(x+\hat{\mu}) \\ &\quad + \bar{d}(x+\hat{\mu})(1+\gamma_\mu)U^\dagger_\mu(x)d(x)\Big]. \end{aligned} \quad \text{(A7)}$$

The conserved current for nHYP fermion has the same form, except the gauge links are nHYP-smeared. Although conserved currents explicitly involve gauge fields and lead to more complicated correlation functions, they have the advantage of circumventing the renormalization issue.

Just like current conservation guarantees the normalization condition in three-point functions,

$$\sum_{\boldsymbol{x}_1}\langle\Omega|\psi(x)j_4^{(q,\mathrm{PS})}(x_1)\psi^\dagger(0)|\Omega\rangle = q_q\langle\Omega|\psi(x)\psi^\dagger(0)|\Omega\rangle, \tag{A8}$$

a similar condition holds in four-point functions,

$$\sum_{\boldsymbol{x}_2,\boldsymbol{x}_1}\langle\Omega|\psi(x)j_4^{(q_2,\mathrm{PS})}(x_2)j_4^{(q_1,\mathrm{PS})}(x_1)\psi^\dagger(0)|\Omega\rangle = q_1q_2\langle\Omega|\psi(x)\psi^\dagger(0)|\Omega\rangle. \tag{A9}$$

In physical terms, the charge overlap at $\boldsymbol{q}=0$ on the left-hand-side is effectively reconstructing the two-point function. Each charge density is spread over all spatial sites on the lattice. By summing over $\boldsymbol{x}_1$ and $\boldsymbol{x}_2$ at zero momentum, we recover the total charge factor from each insertion, regardless of the time points of the insertions. There is a subtle issue with four-point functions. If the two currents couple to different quark lines ($q_1 \neq q_2$), the conservation is for all combinations of t_1 and t_2 between source and sink, including $t_1 = t_2$. If they couple to the same quark line ($q_1 = q_2$), the conservation is only true for $t_1 \neq t_2$. The point $t_1 = t_2$ introduces unwanted contact terms on the lattice and is avoided. The issue is a lattice artifact; in the continuum, the contact interaction is regular and well-defined. The conservation property in Eq. (A9) is used to validate the four-point diagrams in this work.

APPENDIX B: WICK CONTRACTIONS

Here we give the unnormalized correlation functions in Eq. (3) by contracting out all quark-antiqurk pairs.

1. Local current

For point current (PC), using Eqs. (A1) and (A4), the full correlation function has 20 diagrams,

$$\begin{aligned}\tilde{Q}_{\mu\nu}^{(\mathrm{PC})}(\boldsymbol{q},t_3,t_2,t_1,t_0) &= \sum_{\boldsymbol{x}_2,\boldsymbol{x}_1} e^{-i\boldsymbol{q}\cdot\boldsymbol{x}_2}e^{i\boldsymbol{q}\cdot\boldsymbol{x}_1}\sum_{\boldsymbol{x}_3,\boldsymbol{x}_0}\langle\Omega|\psi_{\pi^+}(\boldsymbol{x}_3,t_3)j_\mu^{(\mathrm{PC})}(\boldsymbol{x}_2,t_2)j_\nu^{(\mathrm{PC})}(\boldsymbol{x}_1,t_1)\psi_{\pi^+}^\dagger(\boldsymbol{x}_0,t_0)|\Omega\rangle \\ &\equiv \frac{Z_V^2\kappa^2}{9}\sum_{i=0}^{19} d_i(\boldsymbol{q},t_3,t_2,t_1,t_0),\end{aligned} \tag{B1}$$

where

$$\begin{aligned}
d_{10}^{\mathrm{A}} &= -2\,\mathrm{tr}\Big[S_u(t_1,t_3)\gamma_5 S_d(t_3,t_2)\gamma_\mu e^{-i\mathbf{q}}S_d(t_2,t_0)\gamma_5 S_u(t_0,t_1)\gamma_\nu e^{i\mathbf{q}}\Big],\\
d_7^{\mathrm{A\text{-}bwd}} &= -2\,\mathrm{tr}\Big[S_u(t_2,t_3)\gamma_5 S_d(t_3,t_1)\gamma_\nu e^{i\mathbf{q}}S_d(t_1,t_0)\gamma_5 S_u(t_0,t_2)\gamma_\mu e^{-i\mathbf{q}}\Big],\\
d_5^{\mathrm{B}} &= 4\,\mathrm{tr}\Big[S_u(t_2,t_3)\gamma_5 S_d(t_3,t_0)\gamma_5 S_u(t_0,t_1)\gamma_\nu e^{i\mathbf{q}}S_u(t_1,t_2)\gamma_\mu e^{-i\mathbf{q}}\Big],\\
d_{15}^{\mathrm{B\text{-}bwd}} &= 1\,\mathrm{tr}\Big[S_u(t_0,t_3)\gamma_5 S_d(t_3,t_2)\gamma_\mu e^{-i\mathbf{q}}S_d(t_2,t_1)\gamma_\nu e^{i\mathbf{q}}S_d(t_1,t_0)\gamma_5\Big],\\
d_1^{\mathrm{C}} &= 4\,\mathrm{tr}\Big[S_u(t_1,t_3)\gamma_5 S_d(t_3,t_0)\gamma_5 S_u(t_0,t_2)\gamma_\mu e^{-i\mathbf{q}}S_u(t_2,t_1)\gamma_\nu e^{i\mathbf{q}}\Big],\\
d_{17}^{\mathrm{C\text{-}bwd}} &= 1\,\mathrm{tr}\Big[S_u(t_0,t_3)\gamma_5 S_d(t_3,t_1)\gamma_\nu e^{i\mathbf{q}}S_d(t_1,t_2)\gamma_\mu e^{-i\mathbf{q}}S_d(t_2,t_0)\gamma_5\Big],\\
d_0^{\mathrm{D}} &= -4\,\mathrm{tr}[S_u(t_0,t_3)\gamma_5 S_d(t_3,t_0)\gamma_5]\mathrm{tr}\Big[S_u(t_1,t_2)\gamma_\mu e^{-i\mathbf{q}}S_u(t_2,t_1)\gamma_\nu e^{i\mathbf{q}}\Big],\\
d_{18}^{\mathrm{D}} &= -1\,\mathrm{tr}[S_u(t_0,t_3)\gamma_5 S_d(t_3,t_0)\gamma_5]\mathrm{tr}\Big[S_d(t_1,t_2)\gamma_\mu e^{-i\mathbf{q}}S_d(t_2,t_1)\gamma_\nu e^{i\mathbf{q}}\Big],\\
d_4^{\mathrm{El}} &= -4\,\mathrm{tr}\Big[S_u(t_1,t_3)\gamma_5 S_d(t_3,t_0)\gamma_5 S_u(t_0,t_1)\gamma_\nu e^{i\mathbf{q}}\Big]\mathrm{tr}\Big[S_u(t_2,t_2)\gamma_\mu e^{-i\mathbf{q}}\Big],\\
d_{13}^{\mathrm{El}} &= 2\,\mathrm{tr}\Big[S_u(t_1,t_3)\gamma_5 S_d(t_3,t_0)\gamma_5 S_u(t_0,t_1)\gamma_\nu e^{i\mathbf{q}}\Big]\mathrm{tr}\Big[S_d(t_2,t_2)\gamma_\mu e^{-i\mathbf{q}}\Big],\\
d_6^{\mathrm{El\text{-}bwd}} &= 2\,\mathrm{tr}\Big[S_u(t_0,t_3)\gamma_5 S_d(t_3,t_1)\gamma_\nu e^{i\mathbf{q}}S_d(t_1,t_0)\gamma_5\Big]\mathrm{tr}\Big[S_u(t_2,t_2)\gamma_\mu e^{-i\mathbf{q}}\Big],\\
d_{14}^{\mathrm{El\text{-}bwd}} &= -1\,\mathrm{tr}\Big[S_u(t_0,t_3)\gamma_5 S_d(t_3,t_1)\gamma_\nu e^{i\mathbf{q}}S_d(t_1,t_0)\gamma_5\Big]\mathrm{tr}\Big[S_d(t_2,t_2)\gamma_\mu e^{-i\mathbf{q}}\Big],\\
d_2^{\mathrm{Er}} &= -4\,\mathrm{tr}\Big[S_u(t_2,t_3)\gamma_5 S_d(t_3,t_0)\gamma_5 S_u(t_0,t_2)\gamma_\mu e^{-i\mathbf{q}}\Big]\mathrm{tr}\Big[S_u(t_1,t_1)\gamma_\nu e^{i\mathbf{q}}\Big],
\end{aligned}$$

$$
\begin{aligned}
d_8^{\mathrm{Er}} &= 2\,\mathrm{tr}\Big[S_u(t_2,t_3)\gamma_5 S_d(t_3,t_0)\gamma_5 S_u(t_0,t_2)\gamma_\mu e^{-i\mathbf{q}}\Big]\mathrm{tr}\Big[S_d(t_1,t_1)\gamma_\nu e^{i\mathbf{q}}\Big],\\
d_{11}^{\text{Er-bwd}} &= 2\,\mathrm{tr}\Big[S_u(t_0,t_3)\gamma_5 S_d(t_3,t_2)\gamma_\mu e^{-i\mathbf{q}} S_d(t_2,t_0)\gamma_5\Big]\mathrm{tr}\Big[S_u(t_1,t_1)\gamma_\nu e^{i\mathbf{q}}\Big],\\
d_{16}^{\text{Er-bwd}} &= -1\,\mathrm{tr}\Big[S_u(t_0,t_3)\gamma_5 S_d(t_3,t_2)\gamma_\mu e^{-i\mathbf{q}} S_d(t_2,t_0)\gamma_5\Big]\mathrm{tr}\Big[S_d(t_1,t_1)\gamma_\nu e^{i\mathbf{q}}\Big],\\
d_3^{\mathrm{F}} &= 4\,\mathrm{tr}[S_u(t_0,t_3)\gamma_5 S_d(t_3,t_0)\gamma_5]\mathrm{tr}\Big[S_u(t_2,t_2)\gamma_\mu e^{-i\mathbf{q}}\Big]\mathrm{tr}\Big[S_u(t_1,t_1)\gamma_\nu e^{i\mathbf{q}}\Big],\\
d_9^{\mathrm{F}} &= -2\,\mathrm{tr}[S_u(t_0,t_3)\gamma_5 S_d(t_3,t_0)\gamma_5]\mathrm{tr}\Big[S_u(t_2,t_2)\gamma_\mu e^{-i\mathbf{q}}\Big]\mathrm{tr}\Big[S_d(t_1,t_1)\gamma_\nu e^{i\mathbf{q}}\Big],\\
d_{12}^{\mathrm{F}} &= -2\,\mathrm{tr}[S_u(t_0,t_3)\gamma_5 S_d(t_3,t_0)\gamma_5]\mathrm{tr}\Big[S_d(t_2,t_2)\gamma_\mu e^{-i\mathbf{q}}\Big]\mathrm{tr}\Big[S_u(t_1,t_1)\gamma_\nu e^{i\mathbf{q}}\Big],\\
d_{19}^{\mathrm{F}} &= 1\,\mathrm{tr}[S_u(t_0,t_3)\gamma_5 S_d(t_3,t_0)\gamma_5]\mathrm{tr}\Big[S_d(t_2,t_2)\gamma_\mu e^{-i\mathbf{q}}\Big]\mathrm{tr}\Big[S_d(t_1,t_1)\gamma_\nu e^{i\mathbf{q}}\Big].
\end{aligned}
\tag{B2}
$$

We use a matrix notation that highlights time dependence. The trace is over spin and color. The momentum factor is defined by a diagonal matrix,

$$
[e^{\pm i\mathbf{q}}]_{s,c,\mathbf{x};s',c',\mathbf{x}'} \equiv \delta_{ss'}\delta_{cc'}\delta_{\mathbf{x},\mathbf{x}'}e^{\pm i\mathbf{q}\cdot\mathbf{x}}. \tag{B3}
$$

The spatial sums over $(\boldsymbol{x}_2,\boldsymbol{x}_1,\boldsymbol{x}_3,\boldsymbol{x}_0)$ are implicit in the matrix multiplications. We use $S(t_2,t_1)$ to denote a quark propagator from t_1 to t_2 (from right to left), obtained from the inverse of quark matrix M with a source $Mx = b$, see Eq. (C11). The terms are grouped into six distinct topological diagrams depicted in Fig 2, labeled by superscripts on d_i. If isospin limit ($\kappa_u = \kappa_d = \kappa$) is taken, we get 12 diagrams (first six connected, the rest disconnected),

$$
\begin{aligned}
d_4^{\mathrm{A}} &= -2\,\mathrm{tr}[S(t_1,t_3)\gamma_5 S(t_3,t_2)\gamma_\mu e^{-i\mathbf{q}} S(t_2,t_0)\gamma_5 S(t_0,t_1)\gamma_\nu e^{i\mathbf{q}}],\\
d_2^{\text{A-bwd}} &= -2\,\mathrm{tr}[S(t_2,t_3)\gamma_5 S(t_3,t_1)\gamma_\nu e^{i\mathbf{q}} S(t_1,t_0)\gamma_5 S(t_0,t_2)\gamma_\mu e^{-i\mathbf{q}}],\\
d_1^{\mathrm{B}} &= 4\,\mathrm{tr}[S(t_2,t_3)\gamma_5 S(t_3,t_0)\gamma_5 S(t_0,t_1)\gamma_\nu e^{i\mathbf{q}} S(t_1,t_2)\gamma_\mu e^{-i\mathbf{q}}],\\
d_7^{\text{B-bwd}} &= 1\,\mathrm{tr}[S(t_0,t_3)\gamma_5 S(t_3,t_2)\gamma_\mu e^{-i\mathbf{q}} S(t_2,t_1)\gamma_\nu e^{i\mathbf{q}} S(t_1,t_0)\gamma_5],\\
d_0^{\mathrm{C}} &= 4\,\mathrm{tr}[S(t_1,t_3)\gamma_5 S(t_3,t_0)\gamma_5 S(t_0,t_2)\gamma_\mu e^{-i\mathbf{q}} S(t_2,t_1)\gamma_\nu e^{i\mathbf{q}}],\\
d_9^{\text{C-bwd}} &= 1\,\mathrm{tr}[S(t_0,t_3)\gamma_5 S(t_3,t_1)\gamma_\nu e^{i\mathbf{q}} S(t_1,t_2)\gamma_\mu e^{-i\mathbf{q}} S(t_2,t_0)\gamma_5],\\
d_{10}^{\mathrm{D}} &= -5\,\mathrm{tr}[S(t_0,t_3)\gamma_5 S(t_3,t_0)\gamma_5]\mathrm{tr}[S(t_1,t_2)\gamma_\mu e^{-i\mathbf{q}} S(t_2,t_1)\gamma_\nu e^{i\mathbf{q}}],\\
d_5^{\mathrm{El}} &= -2\,\mathrm{tr}[S(t_1,t_3)\gamma_5 S(t_3,t_0)\gamma_5 S(t_0,t_1)\gamma_\nu e^{i\mathbf{q}}]\mathrm{tr}[S(t_2,t_2)\gamma_\mu e^{-i\mathbf{q}}],\\
d_6^{\text{El-bwd}} &= 1\,\mathrm{tr}[S(t_0,t_3)\gamma_5 S(t_3,t_1)\gamma_\nu e^{i\mathbf{q}} S(t_1,t_0)\gamma_5]\mathrm{tr}[S(t_2,t_2)\gamma_\mu e^{-i\mathbf{q}}],\\
d_3^{\mathrm{Er}} &= -2\,\mathrm{tr}[S(t_2,t_3)\gamma_5 S(t_3,t_0)\gamma_5 S(t_0,t_2)\gamma_\mu e^{-i\mathbf{q}}]\mathrm{tr}[S(t_1,t_1)\gamma_\nu e^{i\mathbf{q}}],\\
d_8^{\text{Er-bwd}} &= 1\,\mathrm{tr}[S(t_0,t_3)\gamma_5 S(t_3,t_2)\gamma_\mu e^{-i\mathbf{q}} S(t_2,t_0)\gamma_5]\mathrm{tr}[S(t_1,t_1)\gamma_\nu e^{i\mathbf{q}}],\\
d_{11}^{\mathrm{F}} &= 1\,\mathrm{tr}[S(t_0,t_3)\gamma_5 S(t_3,t_0)\gamma_5]\mathrm{tr}[S(t_2,t_2)\gamma_\mu e^{-i\mathbf{q}}]\mathrm{tr}[S(t_1,t_1)\gamma_\nu e^{i\mathbf{q}}].
\end{aligned}
\tag{B4}
$$

2. Conserved current

For point-split current (PS), using Eqs. (A1) and (A7), Wick contraction yields 80 diagrams (not shown here) if u and d are distinct. If isospin limit is taken, there are 48 diagrams which we express as

$$
\begin{aligned}
\tilde{Q}_{\mu\nu}^{(\mathrm{PS})}(\boldsymbol{q},t_3,t_2,t_1,t_0) &= \sum_{\boldsymbol{x}_2,\boldsymbol{x}_1} e^{-i\boldsymbol{q}\cdot\boldsymbol{x}_2}e^{i\boldsymbol{q}\cdot\boldsymbol{x}_1}\sum_{\boldsymbol{x}_3,\boldsymbol{x}_0}\langle\Omega|\psi_{\pi^+}(\boldsymbol{x}_3,t_3)j_\mu^{(\mathrm{PS})}(\boldsymbol{x}_2,t_2)j_\nu^{(\mathrm{PS})}(\boldsymbol{x}_1,t_1)\psi_{\pi^+}^\dagger(\boldsymbol{x}_0,t_0)|\Omega\rangle\\
&\equiv \frac{\kappa^2}{9}\sum_{i=0}^{47} d_i(\boldsymbol{q},t_3,t_2,t_1,t_0).
\end{aligned}
\tag{B5}
$$

The 24 connected diagrams are given by

$$
\begin{aligned}
d_{16}^{\mathrm{A}} &= -2\,\mathrm{tr}\Big[S(t_1+\hat{\nu}_4,t_3)(\gamma_5)S(t_3,t_2)(1-\gamma_\mu)e^{-i\mathbf{q}}U_\mu(t_2,t_2+\hat{\mu}_4)S(t_2+\hat{\mu}_4,t_0)(\gamma_5)S(t_0,t_1)(1-\gamma_\nu)e^{i\mathbf{q}}U_\nu(t_1,t_1+\hat{\nu}_4)\Big],\\
d_{18}^{\mathrm{A}} &= 2\,\mathrm{tr}\Big[S(t_1+\hat{\nu}_4,t_3)(\gamma_5)S(t_3,t_2+\hat{\mu}_4)(1+\gamma_\mu)U_\mu^\dagger(t_2+\hat{\mu}_4,t_2)e^{-i\mathbf{q}}S(t_2,t_0)(\gamma_5)S(t_0,t_1)(1-\gamma_\nu)e^{i\mathbf{q}}U_\nu(t_1,t_1+\hat{\nu}_4)\Big],\\
d_{20}^{\mathrm{A}} &= 2\,\mathrm{tr}\Big[S(t_1,t_3)(\gamma_5)S(t_3,t_2)(1-\gamma_\mu)e^{-i\mathbf{q}}U_\mu(t_2,t_2+\hat{\mu}_4)S(t_2+\hat{\mu}_4,t_0)(\gamma_5)S(t_0,t_1+\hat{\nu}_4)(1+\gamma_\nu)U_\nu^\dagger(t_1+\hat{\nu}_4,t_1)e^{i\mathbf{q}}\Big],\\
d_{22}^{\mathrm{A}} &= -2\,\mathrm{tr}\Big[S(t_1,t_3)(\gamma_5)S(t_3,t_2+\hat{\mu}_4)(1+\gamma_\mu)U_\mu^\dagger(t_2+\hat{\mu}_4,t_2)e^{-i\mathbf{q}}S(t_2,t_0)(\gamma_5)S(t_0,t_1+\hat{\nu}_4)(1+\gamma_\nu)U_\nu^\dagger(t_1+\hat{\nu}_4,t_1)e^{i\mathbf{q}}\Big],\\
d_{8}^{\text{A-bwd}} &= -2\,\mathrm{tr}\Big[S(t_2+\hat{\mu}_4,t_3)(\gamma_5)S(t_3,t_1)(1-\gamma_\nu)e^{i\mathbf{q}}U_\nu(t_1,t_1+\hat{\nu}_4)S(t_1+\hat{\nu}_4,t_0)(\gamma_5)S(t_0,t_2)(1-\gamma_\mu)e^{-i\mathbf{q}}U_\mu(t_2,t_2+\hat{\mu}_4)\Big],\\
d_{10}^{\text{A-bwd}} &= 2\,\mathrm{tr}\Big[S(t_2,t_3)(\gamma_5)S(t_3,t_1)(1-\gamma_\nu)e^{i\mathbf{q}}U_\nu(t_1,t_1+\hat{\nu}_4)S(t_1+\hat{\nu}_4,t_0)(\gamma_5)S(t_0,t_2+\hat{\mu}_4)(1+\gamma_\mu)U_\mu^\dagger(t_2+\hat{\mu}_4,t_2)e^{-i\mathbf{q}}\Big],\\
d_{12}^{\text{A-bwd}} &= 2\,\mathrm{tr}\Big[S(t_2+\hat{\mu}_4,t_3)(\gamma_5)S(t_3,t_1+\hat{\nu}_4)(1+\gamma_\nu)U_\nu^\dagger(t_1+\hat{\nu}_4,t_1)e^{i\mathbf{q}}S(t_1,t_0)(\gamma_5)S(t_0,t_2)(1-\gamma_\mu)e^{-i\mathbf{q}}U_\mu(t_2,t_2+\hat{\mu}_4)\Big],\\
d_{14}^{\text{A-bwd}} &= -2\,\mathrm{tr}\Big[S(t_2,t_3)(\gamma_5)S(t_3,t_1+\hat{\nu}_4)(1+\gamma_\nu)U_\nu^\dagger(t_1+\hat{\nu}_4,t_1)e^{i\mathbf{q}}S(t_1,t_0)(\gamma_5)S(t_0,t_2+\hat{\mu}_4)(1+\gamma_\mu)U_\mu^\dagger(t_2+\hat{\mu}_4,t_2)e^{-i\mathbf{q}}\Big],\\
d_{1}^{\mathrm{B}} &= 4\,\mathrm{tr}\Big[S(t_2+\hat{\mu}_4,t_3)(\gamma_5)S(t_3,t_0)(\gamma_5)S(t_0,t_1)(1-\gamma_\nu)e^{i\mathbf{q}}U_\nu(t_1,t_1+\hat{\nu}_4)S(t_1+\hat{\nu}_4,t_2)(1-\gamma_\mu)e^{-i\mathbf{q}}U_\mu(t_2,t_2+\hat{\mu}_4)\Big],\\
d_{3}^{\mathrm{B}} &= -4\,\mathrm{tr}\Big[S(t_2,t_3)(\gamma_5)S(t_3,t_0)(\gamma_5)S(t_0,t_1)(1-\gamma_\nu)e^{i\mathbf{q}}U_\nu(t_1,t_1+\hat{\nu}_4)S(t_1+\hat{\nu}_4,t_2+\hat{\mu}_4)(1+\gamma_\mu)U_\mu^\dagger(t_2+\hat{\mu}_4,t_2)e^{-i\mathbf{q}}\Big],\\
d_{5}^{\mathrm{B}} &= -4\,\mathrm{tr}\Big[S(t_2+\hat{\mu}_4,t_3)(\gamma_5)S(t_3,t_0)(\gamma_5)S(t_0,t_1+\hat{\nu}_4)(1+\gamma_\nu)U_\nu^\dagger(t_1+\hat{\nu}_4,t_1)e^{i\mathbf{q}}S(t_1,t_2)(1-\gamma_\mu)e^{-i\mathbf{q}}U_\mu(t_2,t_2+\hat{\mu}_4)\Big],\\
d_{7}^{\mathrm{B}} &= 4\,\mathrm{tr}\Big[S(t_2,t_3)(\gamma_5)S(t_3,t_0)(\gamma_5)S(t_0,t_1+\hat{\nu}_4)(1+\gamma_\nu)U_\nu^\dagger(t_1+\hat{\nu}_4,t_1)e^{i\mathbf{q}}S(t_1,t_2+\hat{\mu}_4)(1+\gamma_\mu)U_\mu^\dagger(t_2+\hat{\mu}_4,t_2)e^{-i\mathbf{q}}\Big],\\
d_{25}^{\text{B-bwd}} &= 1\,\mathrm{tr}\Big[S(t_0,t_3)(\gamma_5)S(t_3,t_2)(1-\gamma_\mu)e^{-i\mathbf{q}}U_\mu(t_2,t_2+\hat{\mu}_4)S(t_2+\hat{\mu}_4,t_1)(1-\gamma_\nu)e^{i\mathbf{q}}U_\nu(t_1,t_1+\hat{\nu}_4)S(t_1+\hat{\nu}_4,t_0)(\gamma_5)\Big],\\
d_{31}^{\text{B-bwd}} &= -1\,\mathrm{tr}\Big[S(t_0,t_3)(\gamma_5)S(t_3,t_2+\hat{\mu}_4)(1+\gamma_\mu)U_\mu^\dagger(t_2+\hat{\mu}_4,t_2)e^{-i\mathbf{q}}S(t_2,t_1)(1-\gamma_\nu)e^{i\mathbf{q}}U_\nu(t_1,t_1+\hat{\nu}_4)S(t_1+\hat{\nu}_4,t_0)(\gamma_5)\Big],\\
d_{37}^{\text{B-bwd}} &= -1\,\mathrm{tr}\Big[S(t_0,t_3)(\gamma_5)S(t_3,t_2)(1-\gamma_\mu)e^{-i\mathbf{q}}U_\mu(t_2,t_2+\hat{\mu}_4)S(t_2+\hat{\mu}_4,t_1+\hat{\nu}_4)(1+\gamma_\nu)U_\nu^\dagger(t_1+\hat{\nu}_4,t_1)e^{i\mathbf{q}}S(t_1,t_0)(\gamma_5)\Big],\\
d_{43}^{\text{B-bwd}} &= 1\,\mathrm{tr}\Big[S(t_0,t_3)(\gamma_5)S(t_3,t_2+\hat{\mu}_4)(1+\gamma_\mu)U_\mu^\dagger(t_2+\hat{\mu}_4,t_2)e^{-i\mathbf{q}}S(t_2,t_1+\hat{\nu}_4)(1+\gamma_\nu)U_\nu^\dagger(t_1+\hat{\nu}_4,t_1)e^{i\mathbf{q}}S(t_1,t_0)(\gamma_5)\Big],\\
d_{0}^{\mathrm{C}} &= 4\,\mathrm{tr}\Big[S(t_1+\hat{\nu}_4,t_3)(\gamma_5)S(t_3,t_0)(\gamma_5)S(t_0,t_2)(1-\gamma_\mu)e^{-i\mathbf{q}}U_\mu(t_2,t_2+\hat{\mu}_4)S(t_2+\hat{\mu}_4,t_1)(1-\gamma_\nu)e^{i\mathbf{q}}U_\nu(t_1,t_1+\hat{\nu}_4)\Big],\\
d_{2}^{\mathrm{C}} &= -4\,\mathrm{tr}\Big[S(t_1+\hat{\nu}_4,t_3)(\gamma_5)S(t_3,t_0)(\gamma_5)S(t_0,t_2+\hat{\mu}_4)(1+\gamma_\mu)U_\mu^\dagger(t_2+\hat{\mu}_4,t_2)e^{-i\mathbf{q}}S(t_2,t_1)(1-\gamma_\nu)e^{i\mathbf{q}}U_\nu(t_1,t_1+\hat{\nu}_4)\Big],\\
d_{4}^{\mathrm{C}} &= -4\,\mathrm{tr}\Big[S(t_1,t_3)(\gamma_5)S(t_3,t_0)(\gamma_5)S(t_0,t_2)(1-\gamma_\mu)e^{-i\mathbf{q}}U_\mu(t_2,t_2+\hat{\mu}_4)S(t_2+\hat{\mu}_4,t_1+\hat{\nu}_4)(1+\gamma_\nu)U_\nu^\dagger(t_1+\hat{\nu}_4,t_1)e^{i\mathbf{q}}\Big],\\
d_{6}^{\mathrm{C}} &= 4\,\mathrm{tr}\Big[S(t_1,t_3)(\gamma_5)S(t_3,t_0)(\gamma_5)S(t_0,t_2+\hat{\mu}_4)(1+\gamma_\mu)U_\mu^\dagger(t_2+\hat{\mu}_4,t_2)e^{-i\mathbf{q}}S(t_2,t_1+\hat{\nu}_4)(1+\gamma_\nu)U_\nu^\dagger(t_1+\hat{\nu}_4,t_1)e^{i\mathbf{q}}\Big],\\
d_{27}^{\text{C-bwd}} &= 1\,\mathrm{tr}\Big[S(t_0,t_3)(\gamma_5)S(t_3,t_1)(1-\gamma_\nu)e^{i\mathbf{q}}U_\nu(t_1,t_1+\hat{\nu}_4)S(t_1+\hat{\nu}_4,t_2)(1-\gamma_\mu)e^{-i\mathbf{q}}U_\mu(t_2,t_2+\hat{\mu}_4)S(t_2+\hat{\mu}_4,t_0)(\gamma_5)\Big],\\
d_{33}^{\text{C-bwd}} &= -1\,\mathrm{tr}\Big[S(t_0,t_3)(\gamma_5)S(t_3,t_1)(1-\gamma_\nu)e^{i\mathbf{q}}U_\nu(t_1,t_1+\hat{\nu}_4)S(t_1+\hat{\nu}_4,t_2+\hat{\mu}_4)(1+\gamma_\mu)U_\mu^\dagger(t_2+\hat{\mu}_4,t_2)e^{-i\mathbf{q}}S(t_2,t_0)(\gamma_5)\Big],\\
d_{39}^{\text{C-bwd}} &= -1\,\mathrm{tr}\Big[S(t_0,t_3)(\gamma_5)S(t_3,t_1+\hat{\nu}_4)(1+\gamma_\nu)U_\nu^\dagger(t_1+\hat{\nu}_4,t_1)e^{i\mathbf{q}}S(t_1,t_2)(1-\gamma_\mu)e^{-i\mathbf{q}}U_\mu(t_2,t_2+\hat{\mu}_4)S(t_2+\hat{\mu}_4,t_0)(\gamma_5)\Big],\\
d_{45}^{\text{C-bwd}} &= 1\,\mathrm{tr}\Big[S(t_0,t_3)(\gamma_5)S(t_3,t_1+\hat{\nu}_4)(1+\gamma_\nu)U_\nu^\dagger(t_1+\hat{\nu}_4,t_1)e^{i\mathbf{q}}S(t_1,t_2+\hat{\mu}_4)(1+\gamma_\mu)U_\mu^\dagger(t_2+\hat{\mu}_4,t_2)e^{-i\mathbf{q}}S(t_2,t_0)(\gamma_5)\Big].
\end{aligned}
\tag{B6}
$$

The 24 disconnected diagrams are given by

$$
\begin{aligned}
d_{28}^{\mathrm{D}} &= -5\,\mathrm{tr}[S(t_0,t_3)(\gamma_5)S(t_3,t_0)(\gamma_5)]\mathrm{tr}\Big[S(t_1+\hat{\nu}_4,t_2)(1-\gamma_\mu)e^{-i\mathbf{q}}U_\mu(t_2,t_2+\hat{\mu}_4)S(t_2+\hat{\mu}_4,t_1)(1-\gamma_\nu)e^{i\mathbf{q}}U_\nu(t_1,t_1+\hat{\nu}_4)\Big],\\
d_{34}^{\mathrm{D}} &= 5\,\mathrm{tr}[S(t_0,t_3)(\gamma_5)S(t_3,t_0)(\gamma_5)]\mathrm{tr}\Big[S(t_1+\hat{\nu}_4,t_2+\hat{\mu}_4)(1+\gamma_\mu)U_\mu^\dagger(t_2+\hat{\mu}_4,t_2)e^{-i\mathbf{q}}S(t_2,t_1)(1-\gamma_\nu)e^{i\mathbf{q}}U_\nu(t_1,t_1+\hat{\nu}_4)\Big],\\
d_{40}^{\mathrm{D}} &= 5\,\mathrm{tr}[S(t_0,t_3)(\gamma_5)S(t_3,t_0)(\gamma_5)]\mathrm{tr}\Big[S(t_1,t_2)(1-\gamma_\mu)e^{-i\mathbf{q}}U_\mu(t_2,t_2+\hat{\mu}_4)S(t_2+\hat{\mu}_4,t_1+\hat{\nu}_4)(1+\gamma_\nu)U_\nu^\dagger(t_1+\hat{\nu}_4,t_1)e^{i\mathbf{q}}\Big],\\
d_{46}^{\mathrm{D}} &= -5\,\mathrm{tr}[S(t_0,t_3)(\gamma_5)S(t_3,t_0)(\gamma_5)]\mathrm{tr}\Big[S(t_1,t_2+\hat{\mu}_4)(1+\gamma_\mu)U_\mu^\dagger(t_2+\hat{\mu}_4,t_2)e^{-i\mathbf{q}}S(t_2,t_1+\hat{\nu}_4)(1+\gamma_\nu)U_\nu^\dagger(t_1+\hat{\nu}_4,t_1)e^{i\mathbf{q}}\Big],\\
d_{17}^{\mathrm{El}} &= -2\,\mathrm{tr}\Big[S(t_1+\hat{\nu}_4,t_3)(\gamma_5)S(t_3,t_0)(\gamma_5)S(t_0,t_1)(1-\gamma_\nu)e^{i\mathbf{q}}U_\nu(t_1,t_1+\hat{\nu}_4)\Big]\mathrm{tr}\Big[S(t_2+\hat{\mu}_4,t_2)(1-\gamma_\mu)e^{-i\mathbf{q}}U_\mu(t_2,t_2+\hat{\mu}_4)\Big],\\
d_{19}^{\mathrm{El}} &= 2\,\mathrm{tr}\Big[S(t_1+\hat{\nu}_4,t_3)(\gamma_5)S(t_3,t_0)(\gamma_5)S(t_0,t_1)(1-\gamma_\nu)e^{i\mathbf{q}}U_\nu(t_1,t_1+\hat{\nu}_4)\Big]\mathrm{tr}\Big[S(t_2,t_2+\hat{\mu}_4)(1+\gamma_\mu)U_\mu^\dagger(t_2+\hat{\mu}_4,t_2)e^{-i\mathbf{q}}\Big],\\
d_{21}^{\mathrm{El}} &= 2\,\mathrm{tr}\Big[S(t_1,t_3)(\gamma_5)S(t_3,t_0)(\gamma_5)S(t_0,t_1+\hat{\nu}_4)(1+\gamma_\nu)U_\nu^\dagger(t_1+\hat{\nu}_4,t_1)e^{i\mathbf{q}}\Big]\mathrm{tr}\Big[S(t_2+\hat{\mu}_4,t_2)(1-\gamma_\mu)e^{-i\mathbf{q}}U_\mu(t_2,t_2+\hat{\mu}_4)\Big],\\
d_{23}^{\mathrm{El}} &= -2\,\mathrm{tr}\Big[S(t_1,t_3)(\gamma_5)S(t_3,t_0)(\gamma_5)S(t_0,t_1+\hat{\nu}_4)(1+\gamma_\nu)U_\nu^\dagger(t_1+\hat{\nu}_4,t_1)e^{i\mathbf{q}}\Big]\mathrm{tr}\Big[S(t_2,t_2+\hat{\mu}_4)(1+\gamma_\mu)U_\mu^\dagger(t_2+\hat{\mu}_4,t_2)e^{-i\mathbf{q}}\Big],\\
d_{24}^{\text{El-bwd}} &= 1\,\mathrm{tr}\Big[S(t_0,t_3)(\gamma_5)S(t_3,t_1)(1-\gamma_\nu)e^{i\mathbf{q}}U_\nu(t_1,t_1+\hat{\nu}_4)S(t_1+\hat{\nu}_4,t_0)(\gamma_5)\Big]\mathrm{tr}\Big[S(t_2+\hat{\mu}_4,t_2)(1-\gamma_\mu)e^{-i\mathbf{q}}U_\mu(t_2,t_2+\hat{\mu}_4)\Big],\\
d_{30}^{\text{El-bwd}} &= -1\,\mathrm{tr}\Big[S(t_0,t_3)(\gamma_5)S(t_3,t_1)(1-\gamma_\nu)e^{i\mathbf{q}}U_\nu(t_1,t_1+\hat{\nu}_4)S(t_1+\hat{\nu}_4,t_0)(\gamma_5)\Big]\mathrm{tr}\Big[S(t_2,t_2+\hat{\mu}_4)(1+\gamma_\mu)U_\mu^\dagger(t_2+\hat{\mu}_4,t_2)e^{-i\mathbf{q}}\Big],\\
d_{36}^{\text{El-bwd}} &= -1\,\mathrm{tr}\Big[S(t_0,t_3)(\gamma_5)S(t_3,t_1+\hat{\nu}_4)(1+\gamma_\nu)U_\nu^\dagger(t_1+\hat{\nu}_4,t_1)e^{i\mathbf{q}}S(t_1,t_0)(\gamma_5)\Big]\mathrm{tr}\Big[S(t_2+\hat{\mu}_4,t_2)(1-\gamma_\mu)e^{-i\mathbf{q}}U_\mu(t_2,t_2+\hat{\mu}_4)\Big],\\
d_{42}^{\text{El-bwd}} &= 1\,\mathrm{tr}\Big[S(t_0,t_3)(\gamma_5)S(t_3,t_1+\hat{\nu}_4)(1+\gamma_\nu)U_\nu^\dagger(t_1+\hat{\nu}_4,t_1)e^{i\mathbf{q}}S(t_1,t_0)(\gamma_5)\Big]\mathrm{tr}\Big[S(t_2,t_2+\hat{\mu}_4)(1+\gamma_\mu)U_\mu^\dagger(t_2+\hat{\mu}_4,t_2)e^{-i\mathbf{q}}\Big],\\
d_{9}^{\mathrm{Er}} &= -2\,\mathrm{tr}\Big[S(t_2+\hat{\mu}_4,t_3)(\gamma_5)S(t_3,t_0)(\gamma_5)S(t_0,t_2)(1-\gamma_\mu)e^{-i\mathbf{q}}U_\mu(t_2,t_2+\hat{\mu}_4)\Big]\mathrm{tr}\Big[S(t_1+\hat{\nu}_4,t_1)(1-\gamma_\nu)e^{i\mathbf{q}}U_\nu(t_1,t_1+\hat{\nu}_4)\Big],\\
d_{11}^{\mathrm{Er}} &= 2\,\mathrm{tr}\Big[S(t_2,t_3)(\gamma_5)S(t_3,t_0)(\gamma_5)S(t_0,t_2+\hat{\mu}_4)(1+\gamma_\mu)U_\mu^\dagger(t_2+\hat{\mu}_4,t_2)e^{-i\mathbf{q}}\Big]\mathrm{tr}\Big[S(t_1+\hat{\nu}_4,t_1)(1-\gamma_\nu)e^{i\mathbf{q}}U_\nu(t_1,t_1+\hat{\nu}_4)\Big],\\
d_{13}^{\mathrm{Er}} &= 2\,\mathrm{tr}\Big[S(t_2+\hat{\mu}_4,t_3)(\gamma_5)S(t_3,t_0)(\gamma_5)S(t_0,t_2)(1-\gamma_\mu)e^{-i\mathbf{q}}U_\mu(t_2,t_2+\hat{\mu}_4)\Big]\mathrm{tr}\Big[S(t_1,t_1+\hat{\nu}_4)(1+\gamma_\nu)U_\nu^\dagger(t_1+\hat{\nu}_4,t_1)e^{i\mathbf{q}}\Big],\\
d_{15}^{\mathrm{Er}} &= -2\,\mathrm{tr}\Big[S(t_2,t_3)(\gamma_5)S(t_3,t_0)(\gamma_5)S(t_0,t_2+\hat{\mu}_4)(1+\gamma_\mu)U_\mu^\dagger(t_2+\hat{\mu}_4,t_2)e^{-i\mathbf{q}}\Big]\mathrm{tr}\Big[S(t_1,t_1+\hat{\nu}_4)(1+\gamma_\nu)U_\nu^\dagger(t_1+\hat{\nu}_4,t_1)e^{i\mathbf{q}}\Big],\\
d_{26}^{\text{Er-bwd}} &= 1\,\mathrm{tr}\Big[S(t_0,t_3)(\gamma_5)S(t_3,t_2)(1-\gamma_\mu)e^{-i\mathbf{q}}U_\mu(t_2,t_2+\hat{\mu}_4)S(t_2+\hat{\mu}_4,t_0)(\gamma_5)\Big]\mathrm{tr}\Big[S(t_1+\hat{\nu}_4,t_1)(1-\gamma_\nu)e^{i\mathbf{q}}U_\nu(t_1,t_1+\hat{\nu}_4)\Big],\\
d_{32}^{\text{Er-bwd}} &= -1\,\mathrm{tr}\Big[S(t_0,t_3)(\gamma_5)S(t_3,t_2+\hat{\mu}_4)(1+\gamma_\mu)U_\mu^\dagger(t_2+\hat{\mu}_4,t_2)e^{-i\mathbf{q}}S(t_2,t_0)(\gamma_5)\Big]\mathrm{tr}\Big[S(t_1+\hat{\nu}_4,t_1)(1-\gamma_\nu)e^{i\mathbf{q}}U_\nu(t_1,t_1+\hat{\nu}_4)\Big],\\
d_{38}^{\text{Er-bwd}} &= -1\,\mathrm{tr}\Big[S(t_0,t_3)(\gamma_5)S(t_3,t_2)(1-\gamma_\mu)e^{-i\mathbf{q}}U_\mu(t_2,t_2+\hat{\mu}_4)S(t_2+\hat{\mu}_4,t_0)(\gamma_5)\Big]\mathrm{tr}\Big[S(t_1,t_1+\hat{\nu}_4)(1+\gamma_\nu)U_\nu^\dagger(t_1+\hat{\nu}_4,t_1)e^{i\mathbf{q}}\Big],\\
d_{44}^{\text{Er-bwd}} &= 1\,\mathrm{tr}\Big[S(t_0,t_3)(\gamma_5)S(t_3,t_2+\hat{\mu}_4)(1+\gamma_\mu)U_\mu^\dagger(t_2+\hat{\mu}_4,t_2)e^{-i\mathbf{q}}S(t_2,t_0)(\gamma_5)\Big]\mathrm{tr}\Big[S(t_1,t_1+\hat{\nu}_4)(1+\gamma_\nu)U_\nu^\dagger(t_1+\hat{\nu}_4,t_1)e^{i\mathbf{q}}\Big],\\
d_{29}^{\mathrm{F}} &= 1\,\mathrm{tr}[S(t_0,t_3)(\gamma_5)S(t_3,t_0)(\gamma_5)]\mathrm{tr}\Big[S(t_2+\hat{\mu}_4,t_2)(1-\gamma_\mu)e^{-i\mathbf{q}}U_\mu(t_2,t_2+\hat{\mu}_4)\Big]\mathrm{tr}\Big[S(t_1+\hat{\nu}_4,t_1)(1-\gamma_\nu)e^{i\mathbf{q}}U_\nu(t_1,t_1+\hat{\nu}_4)\Big],\\
d_{35}^{\mathrm{F}} &= -1\,\mathrm{tr}[S(t_0,t_3)(\gamma_5)S(t_3,t_0)(\gamma_5)]\mathrm{tr}\Big[S(t_2,t_2+\hat{\mu}_4)(1+\gamma_\mu)U_\mu^\dagger(t_2+\hat{\mu}_4,t_2)e^{-i\mathbf{q}}\Big]\mathrm{tr}\Big[S(t_1+\hat{\nu}_4,t_1)(1-\gamma_\nu)e^{i\mathbf{q}}U_\nu(t_1,t_1+\hat{\nu}_4)\Big],\\
d_{41}^{\mathrm{F}} &= -1\,\mathrm{tr}[S(t_0,t_3)(\gamma_5)S(t_3,t_0)(\gamma_5)]\mathrm{tr}\Big[S(t_2+\hat{\mu}_4,t_2)(1-\gamma_\mu)e^{-i\mathbf{q}}U_\mu(t_2,t_2+\hat{\mu}_4)\Big]\mathrm{tr}\Big[S(t_1,t_1+\hat{\nu}_4)(1+\gamma_\nu)U_\nu^\dagger(t_1+\hat{\nu}_4,t_1)e^{i\mathbf{q}}\Big],\\
d_{47}^{\mathrm{F}} &= 1\,\mathrm{tr}[S(t_0,t_3)(\gamma_5)S(t_3,t_0)(\gamma_5)]\mathrm{tr}\Big[S(t_2,t_2+\hat{\mu}_4)(1+\gamma_\mu)U_\mu^\dagger(t_2+\hat{\mu}_4,t_2)e^{-i\mathbf{q}}\Big]\mathrm{tr}\Big[S(t_1,t_1+\hat{\nu}_4)(1+\gamma_\nu)U_\nu^\dagger(t_1+\hat{\nu}_4,t_1)e^{i\mathbf{q}}\Big].
\end{aligned}
\tag{B7}
$$

The shifted quark propagators have the following meaning depending on whether the current is split in temporal or spatial directions, for example,

$$S(t_3, t_2+\hat{\mu}_4) \equiv \begin{cases} S(t_3, t_2+1) = P(t_3)M^{-1}P(t_2+1)^T, & \text{if } \mu = 4 \\ S(t_3, t_2) = P(t_3)M^{-1}P(t_2)^T, & \text{if } \mu \neq 4, \end{cases} \tag{B8}$$

where the projector $P(t)$ is defined in Eq. (C9). The associated gauge links have the meaning,

$$\begin{aligned} U_\mu(t_2, t_2+\hat{\mu}_4) &\equiv \begin{cases} U_4(t_2, t_2+1), & \text{if } \mu = 4 \\ U_\mu(t_2, t_2), & \text{if } \mu \neq 4, \end{cases} \\ U_\mu^\dagger(t_2+\hat{\mu}_4, t_2) &\equiv \begin{cases} U_4^\dagger(t_2+1, t_2), & \text{if } \mu = 4 \\ U_\mu^\dagger(t_2, t_2), & \text{if } \mu \neq 4, \end{cases} \end{aligned} \tag{B9}$$

where the gauge links are defined in Eq. (C6). So the split in time is explicitly carried in both the propagators and gauge links, whereas the split in space is only implicitly carried in the gauge links. Note the placement of $e^{\pm iq}$ in relation to U and $U^\dagger$. They do not commute when the currents are split in spatial directions.

APPENDIX C: WALL SOURCE IMPLEMENTATION

We introduce a rigorous matrix notation to elucidate the implementation of wall sources. We define wall sources as a vector in spatial coordinates, diagonal in spin and color,

$$[\mathcal{W}]_{s,c,\mathbf{x};s',c'} \equiv \delta_{ss'}\delta_{cc'}. \tag{C1}$$

That is, all spatial entries of the real part are set to 1, imaginary part to zero. It can be placed at any time slice. Under a gauge transformation G, the gauge average is

$$\langle G(t)\mathcal{W}\mathcal{W}^T G(t)^\dagger\rangle_G = \mathbb{1}_{\boldsymbol{x},s,c}, \quad \text{where } [G(t)\mathcal{W}]_{\mathbf{x}} = G(t,\mathbf{x})\mathbb{1}_{\mathbf{s},\mathbf{c}}. \tag{C2}$$

More explicitly,

$$[\langle G(t)\mathcal{W}\mathcal{W}^T G(t)^\dagger\rangle_G]_{\boldsymbol{x}\boldsymbol{y}} = \frac{1}{|G|}\int DG G(t,\boldsymbol{x})\mathbb{1}_{\text{spin}} G(t,\boldsymbol{y})^\dagger \mathbb{1}_{\text{spin}} = \delta_{\boldsymbol{x}\boldsymbol{y}}\mathbb{1}_s\mathbb{1}_c. \tag{C3}$$

We insert the wall source in between a pair of quark propagators in the path integral by the following steps, only highlighting the time dependence in S to keep the notation simple,

$$\begin{aligned} &\int DUP(U) \operatorname*{Tr}_{\boldsymbol{x},s,c}\Big[\ldots S[U](t',t)S[U](t,t'')\ldots\Big] \\ &= \int DUP(U) \operatorname*{Tr}_{\boldsymbol{x},s,c}\Big[\ldots S[U](t',t)\mathbb{1}_{\boldsymbol{x},s,c}S[U](t,t'')\ldots\Big] \\ &= \frac{1}{|G|}\int DG \int DUP(U) \operatorname*{Tr}_{\boldsymbol{x},s,c}\Big[\ldots S[U](t',t)G(t)\mathcal{W}\mathcal{W}^T G(t)^\dagger S[U](t,t'')\ldots\Big] \\ &= \frac{1}{|G|}\int DG \int DUP(U_G) \operatorname*{Tr}_{\boldsymbol{x},s,c}\Big[\ldots S[U_G](t',t)G(t)\mathcal{W}\mathcal{W}^T G(t)^\dagger S[U_G](t,t'')\ldots\Big] \\ &= \frac{1}{|G|}\int DG \int DUP(U) \operatorname*{Tr}_{\boldsymbol{x},s,c}\Big[\ldots S[U](t',t)\mathcal{W}\mathcal{W}^T S[U](t,t'')\ldots\Big] \\ &= \int DUP(U) \operatorname*{Tr}_{\boldsymbol{x},s,c}\Big[\ldots S[U](t',t)\mathcal{W}\mathcal{W}^T S[U](t,t'')\ldots\Big] \\ &= \int DUP(U) \operatorname*{Tr}_{s,c}\Big[\mathcal{W}^T S[U](t,t'')\ldots S[U](t',t)\mathcal{W}\Big]. \end{aligned} \tag{C4}$$

In the last step, we use the cyclic property of trace $\mathrm{Tr}AB = \mathrm{Tr}BA$. We also used the property that under a gauge transformation $U_\mu \to (U_G)_\mu \equiv GU_\mu G^\dagger$, the propagator transforms as

$$S[U_G](t,t') = G(t)S[U](t,t')G(t')^\dagger. \tag{C5}$$

More explicitly, the gauge links are

$$(U_\mu)_{\boldsymbol{x},t;\boldsymbol{x}',t'} = \delta_{(\boldsymbol{x},t),(\boldsymbol{x}',t')-\mu} U_\mu(\boldsymbol{x},t)\mathbb{1}_s, \tag{C6}$$

and its gauge transformation is

$$\begin{aligned}(GU_\mu G^\dagger)_{x,y} &= G(x)[U_\mu]_{x,y}G(y)^\dagger = G(x)\delta_{x,y-\mu}U_\mu(x)G(y)^\dagger \\ &= \delta_{x,y-\mu}G(x)U_\mu(x)G(x+\mu)^\dagger.\end{aligned} \tag{C7}$$

Note that we will use

$$U_\mu(t,t') = P(t)U_\mu P(t')^T \quad \text{and} \quad U_\mu^\dagger(t,t') = P(t)U_\mu^\dagger P(t')^T. \tag{C8}$$

Here $P(t)$ is defined as projection to a time slice [not to be confused with the weighting factor $P(U)$ in the path integral in Eq. (C4)],

$$[P(t_p)]_{s,c,\mathbf{x};s',c',t',\mathbf{x}'} \equiv \delta_{t_p,t'}\delta_{ss'}\delta_{cc'}\delta_{\mathbf{x},\mathbf{x}'}, \tag{C9}$$

which is diagonal in spin, color, and space. When we take the dagger of $U_\mu(t,t')$, we need to switch the time arguments since

$$\begin{aligned}[U_\mu(t,t')]^\dagger &= [P(t)U_\mu P(t')^T]^\dagger = P(t')U_\mu^\dagger P(t)^T \\ &= U_\mu^\dagger(t',t).\end{aligned} \tag{C10}$$

Operationally, a quark propagator can be written in terms of the inverse of the quark matrix as

$$S(t,t') \equiv P(t)M_q^{-1}P(t')^T. \tag{C11}$$

For Wilson-type fermions, M_q satisfies the γ_5-hermiticity relation

$$M_q^\dagger = \gamma_5 M_q \gamma_5, \qquad (M_q^{-1})^\dagger = \gamma_5 M_q^{-1}\gamma_5. \tag{C12}$$

Examples on how to use the notation to calculate two-point and four-point correlation functions are discussed in Sec. III.

APPENDIX D: FORM FACTOR FROM FOUR-POINT FUNCTIONS

TABLE II. Pion form factor $F_\pi(\boldsymbol{q}^2)$ from four-point functions. An example of the data to be fitted is given in Fig. 8. The fit form is in Eq. (8) with F_π and E_π treated as free parameters and m_π taken from the measured value. For comparison, the E_π from the continuum dispersion relation is provided with the same m_π values. The four columns correspond to $\boldsymbol{q} = \{0,0,1\}, \{0,1,1\}, \{1,1,1\}, \{0,0,2\}$, from left to right.

		$m_\pi = 1100$ MeV		
F_π	0.8209 ± 0.0023	0.7213 ± 0.0023	0.650 ± 0.004	0.604 ± 0.005
E_π fit	1.2556 ± 0.0016	1.4021 ± 0.0027	1.530 ± 0.004	1.644 ± 0.006
E_π continuum	1.2597 ± 0.0010	1.3976 ± 0.0009	1.5230 ± 0.0009	1.6389 ± 0.0008
Fit range	$\{7,9\}$	$\{6,8\}$	$\{7,10\}$	$\{7,12\}$
χ^2/dof	2.00	1.40	2.70	1.90
		$m_\pi = 800$ MeV		
F_π	0.7677 ± 0.0027	0.646 ± 0.006	0.568 ± 0.010	0.552 ± 0.011
E_π fit	0.9967 ± 0.0020	1.163 ± 0.005	1.308 ± 0.010	1.463 ± 0.013
E_π continuum	0.9992 ± 0.0009	1.1682 ± 0.0007	1.3157 ± 0.0007	1.4483 ± 0.0006
Fit range	$\{9,13\}$	$\{10,17\}$	$\{10,17\}$	$\{9,14\}$
χ^2/dof	1.40	1.40	1.10	0.72
		$m_\pi = 600$ MeV		
F_π	0.7412 ± 0.0015	0.6360 ± 0.0025	0.583 ± 0.004	0.525 ± 0.012
E_π fit	0.8508 ± 0.0017	1.050 ± 0.004	1.231 ± 0.007	1.354 ± 0.016
E_π continuum	0.8500 ± 0.0010	1.0435 ± 0.0008	1.2063 ± 0.0007	1.3497 ± 0.0006
Fit range	$\{4,13\}$	$\{6,15\}$	$\{6,9\}$	$\{8,13\}$
χ^2/dof	0.52	1.30	1.50	0.39
		$m_\pi = 360$ MeV		
F_π	0.720 ± 0.004	0.616 ± 0.005	0.554 ± 0.006	0.530 ± 0.008
E_π fit	0.695 ± 0.005	0.911 ± 0.009	1.076 ± 0.013	1.258 ± 0.018
E_π continuum	0.7082 ± 0.0011	0.9316 ± 0.0009	1.1110 ± 0.0007	1.2652 ± 0.0006
Fit range	$\{6,11\}$	$\{6,11\}$	$\{6,11\}$	$\{6,11\}$
χ^2/dof	0.68	0.34	0.68	1.00

[1] H. R. Fiebig, W. Wilcox, and R. M. Woloshyn, A study of hadron electric polarizability in quenched lattice QCD, Nucl. Phys. **B324**, 47 (1989).

[2] M. Lujan, A. Alexandru, W. Freeman, and F. X. Lee, Finite volume effects on the electric polarizability of neutral hadrons in lattice QCD, Phys. Rev. D **94**, 074506 (2016).

[3] Michael Lujan, Andrei Alexandru, Walter Freeman, and Frank Lee, Electric polarizability of neutral hadrons from dynamical lattice QCD ensembles, Phys. Rev. D **89**, 074506 (2014).

[4] Walter Freeman, Andrei Alexandru, Michael Lujan, and Frank X. Lee, Sea quark contributions to the electric polarizability of hadrons, Phys. Rev. D **90**, 054507 (2014).

[5] Walter Freeman, Andrei Alexandru, Frank X. Lee, and Mike Lujan, Update on the sea contributions to hadron electric polarizabilities through reweighting, in *Proceedings of the 31st International Symposium on Lattice Field Theory* (2013), arXiv:1310.4426.

[6] Brian C. Tiburzi, Hadrons in strong electric and magnetic fields, Nucl. Phys. **A814**, 74 (2008).

[7] William Detmold, Brian C. Tiburzi, and Andre Walker-Loud, Lattice QCD in background fields, *Proceedings, 10th Workshop on Non-Perturbative Quantum Chromodynamics: Paris, France, 2009* (2009), arXiv:0908.3626.

[8] Andrei Alexandru and Frank X. Lee, The background field method on the lattice, Proc. Sci. LATTICE2008 (**2008**) 145.

[9] Frank X. Lee, Leming Zhou, Walter Wilcox, and Joseph C. Christensen, Magnetic polarizability of hadrons from lattice QCD in the background field method, Phys. Rev. D **73**, 034503 (2006).

[10] F. X. Lee, R. Kelly, L. Zhou, and W. Wilcox, Baryon magnetic moments in the background field method, Phys. Lett. B **627**, 71 (2005).

[11] Michael Engelhardt, Neutron electric polarizability from unquenched lattice QCD using the background field approach, Phys. Rev. D **76**, 114502 (2007).

[12] Ryan Bignell, Waseem Kamleh, and Derek Leinweber, Magnetic polarizability of the nucleon using a Laplacian mode projection, Phys. Rev. D **101**, 094502 (2020).

[13] Amol Deshmukh and Brian C. Tiburzi, Octet baryons in large magnetic fields, Phys. Rev. D **97**, 014006 (2018).

[14] Gunnar S. Bali, Bastian B. Brandt, Gergely Endrődi, and Benjamin Gläßle, Meson masses in electromagnetic fields with Wilson fermions, Phys. Rev. D **97**, 034505 (2018).

[15] F. Bruckmann, G. Endrodi, M. Giordano, S. D. Katz, T. G. Kovacs, F. Pittler, and J. Wellnhofer, Landau levels in QCD, Phys. Rev. D **96**, 074506 (2017).

[16] Assumpta Parreno, Martin J. Savage, Brian C. Tiburzi, Jonas Wilhelm, Emmanuel Chang, William Detmold, and Kostas Orginos, Octet baryon magnetic moments from lattice QCD: Approaching experiment from a three-flavor symmetric point, Phys. Rev. D **95**, 114513 (2017).

[17] E. V. Luschevskaya, O. E. Solovjeva, and O. V. Teryaev, Magnetic polarizability of pion, Phys. Lett. B **761**, 393 (2016).

[18] Emmanuel Chang, William Detmold, Kostas Orginos, Assumpta Parreno, Martin J. Savage, Brian C. Tiburzi, and Silas R. Beane (NPLQCD Collaboration), Magnetic structure of light nuclei from lattice QCD, Phys. Rev. D **92**, 114502 (2015).

[19] W. Detmold, B. C. Tiburzi, and A. Walker-Loud, Extracting nucleon magnetic moments and electric polarizabilities from lattice QCD in background electric fields, Phys. Rev. D **81**, 054502 (2010).

[20] Zohreh Davoudi and William Detmold, Implementation of general background electromagnetic fields on a periodic hypercubic lattice, Phys. Rev. D **92**, 074506 (2015).

[21] Michael Engelhardt, Exploration of the electric spin polarizability of the neutron in lattice QCD, Proc. Sci. LATTICE2011 (**2011**) 153.

[22] Frank X. Lee and Andrei Alexandru, Spin polarizabilities on the lattice, Proc. Sci. LATTICE2011 (**2011**) 317.

[23] W. Detmold, B. C. Tiburzi, and Andre Walker-Loud, Electromagnetic and spin polarisabilities in lattice QCD, Phys. Rev. D **73**, 114505 (2006).

[24] W. Detmold, B. C. Tiburzi, and A. Walker-Loud, Extracting electric polarizabilities from lattice QCD, Phys. Rev. D **79**, 094505 (2009).

[25] Hossein Niyazi, Andrei Alexandru, Frank X. Lee, and Michael Lujan, Charged pion electric polarizability from lattice QCD, Phys. Rev. D **104**, 014510 (2021).

[26] Ryan Bignell, Waseem Kamleh, and Derek Leinweber, Pion magnetic polarisability using the background field method, Phys. Lett. B **811**, 135853 (2020).

[27] Fangcheng He, Derek B. Leinweber, Anthony W. Thomas, and Ping Wang, Chiral extrapolation of the charged-pion magnetic polarizability with Padé approximant, Phys. Rev. D **104**, 054506 (2021).

[28] Jian Liang, Terrence Draper, Keh-Fei Liu, Alexander Rothkopf, and Yi-Bo Yang (XQCD Collaboration), Towards the nucleon hadronic tensor from lattice QCD, Phys. Rev. D **101**, 114503 (2020).

[29] Jian Liang and Keh-Fei Liu, PDFS and neutrino-nucleon scattering from hadronic tensor, Proc. Sci. LATTICE2019 (**2020**) 046.

[30] Ziwen Fu, Lattice study on πk scattering with moving wall source, Phys. Rev. D **85**, 074501 (2012).

[31] C. Alexandrou, Hadron deformation from lattice QCD, Nucl. Phys. B, Proc. Suppl. **128**, 1 (2004).

[32] Gunnar S. Bali, Peter C. Bruns, Luca Castagnini, Markus Diehl, Jonathan R. Gaunt, Benjamin Gläßle, Andreas Schäfer, André Sternbeck, and Christian Zimmermann, Two-current correlations in the pion on the lattice, J. High Energy Phys. 02 (2018) 061.

[33] Gunnar S. Bali, Markus Diehl, Benjamin Gläßle, Andreas Schäfer, and Christian Zimmermann, Double parton distributions in the nucleon from lattice QCD, J. High Energy Phys. 09 (2021) 106.

[34] M. Burkardt, J. M. Grandy, and J. W. Negele, Calculation and interpretation of hadron correlation functions in lattice QCD, Ann. Phys. (N.Y.) **238**, 441 (1995).

[35] Walter Wilcox, Lattice charge overlap. 2: Aspects of charged pion polarizability, Ann. Phys. (N.Y.) **255**, 60 (1997).

[36] Xu Feng, Taku Izubuchi, Luchang Jin, and Maarten Golterman, Pion electric polarizabilities from lattice QCD, Proc. Sci. LATTICE2021 (**2022**) 362.

[37] X. H. Wang, X. Feng, and L. C. Jin, *Lattice QCD calculation of the proton electromagnetic polarizability, LATTICE2021 proceedings* (2022).
[38] Walter Wilcox and Frank X. Lee, Towards charged hadron polarizabilities from four-point functions in lattice QCD, Phys. Rev. D **104**, 034506 (2021).
[39] M. A. Ivanov and T. Mizutani, Pion and kaon polarizabilities in the quark confinement model, Phys. Rev. D **45**, 1580 (1992).
[40] A. E. Dorokhov, M. K. Volkov, J. Hüfner, S. P. Klevansky, and P. Rehberg, Pion polarizabilities at finite temperature, Z. Phys. C Part. Fields **75**, 127 (1997).
[41] Véronique Bernard and D. Vautherin, Electromagnetic polarizabilities of pseudoscalar goldstone bosons, Phys. Rev. D **40**, 1615 (1989).
[42] Véronique Bernard, Brigitte Hiller, and Wolfram Weise, Pion electromagnetic polarizability and chiral models, Phys. Lett. B **205**, 16 (1988).
[43] A. I. L'vov, Theoretical aspects of the polarizability of the nucleon, Int. J. Mod. Phys. A **08**, 5267 (1993).
[44] A. I. L'vov, S. Scherer, B. Pasquini, C. Unkmeir, and D. Drechsel, Generalized dipole polarizabilities and the spatial structure of hadrons, Phys. Rev. C **64**, 015203 (2001).
[45] B. Pasquini, D. Drechsel, and S. Scherer, Reply to "comment on 'polarizability of the pion: No conflict between dispersion theory and chiral perturbation theory'", Phys. Rev. C **81**, 029802 (2010).
[46] L. V. Fil'kov and V. L. Kashevarov, Dipole polarizabilities of charged pions, Phys. Part. Nucl. **48**, 117 (2017).
[47] Murray Moinester and Stefan Scherer, Compton scattering off pions and electromagnetic polarizabilities, Int. J. Mod. Phys. A **34**, 1930008 (2019).
[48] Vadim Lensky and Vladimir Pascalutsa, Predictive powers of chiral perturbation theory in Compton scattering off protons, Eur. Phys. J. C **65**, 195 (2010).
[49] Franziska Hagelstein, Nucleon polarizabilities and compton scattering as a playground for chiral perturbation theory, Symmetry **12**, 1407 (2020).
[50] J. A. McGovern, D. R. Phillips, and H. W. Griesshammer, Compton scattering from the proton in an effective field theory with explicit Delta degrees of freedom, Eur. Phys. J. A **49**, 12 (2013).
[51] H. W. Griesshammer, J. A. McGovern, D. R. Phillips, and G. Feldman, Using effective field theory to analyse low-energy Compton scattering data from protons and light nuclei, Prog. Part. Nucl. Phys. **67**, 841 (2012).
[52] Murray Moinester, Pion polarizability 2022 status report, arXiv:2205.09954.
[53] Terrence Draper, R. M. Woloshyn, Walter Wilcox, and Keh-Fei Liu, The pion form-factor in lattice QCD, Nucl. Phys. **B318**, 319 (1989).
[54] Y. Kuramashi, M. Fukugita, H. Mino, M. Okawa, and A. Ukawa, Lattice QCD Calculation of Full Pion Scattering Lengths, Phys. Rev. Lett. **71**, 2387 (1993).
[55] S. Cabasino *et al.*, $\beta = 6.0$ quenched wilson fermions, Phys. Lett. B **258**, 195 (1991).
[56] G. Martinelli and C. T. Sachrajda, A lattice calculation of the pion's form factor and structure function, Nucl. Phys. **B306**, 865 (1988).
[57] Gabriel Lee, John R. Arrington, and Richard J. Hill, Extraction of the proton radius from electron-proton scattering data, Phys. Rev. D **92**, 013013 (2015).
[58] J. van der Heide, J. H. Koch, and E. Laermann, Pion structure from improved lattice QCD: Form factor and charge radius at low masses, Phys. Rev. D **69**, 094511 (2004).
[59] J. Gasser, M. A. Ivanov, and M. E. Sainio, Revisiting $\gamma\gamma \to \pi^+\pi^-$ at low energies, Nucl. Phys. **B745**, 84 (2006).
[60] R. L. Workman *et al.* (Particle Data Group), Review of particle physics, Prog. Theor. Exp. Phys. **2022**, 083C01 (2022).
[61] A. Alexandru, C. Pelissier, B. Gamari, and F. Lee, Multi-mass solvers for lattice QCD on GPUs, J. Comput. Phys. **231**, 1866 (2012).
[62] Hossein Niyazi, Andrei Alexandru, Frank X. Lee, and Ruairí Brett, Setting the scale for nHYP fermions with the Lüscher-Weisz gauge action, Phys. Rev. D **102**, 094506 (2020).
[63] Luuk H Karsten and Jan Smith, Lattice fermions: Species doubling, chiral invariance and the triangle anomaly, Nucl. Phys. **B183**, 103 (1981).
[64] Christof Gattringer and Christian B. Lang, *Quantum Chromodynamics on the Lattice* (Springer, Berlin, 2010), Vol. 788.
[65] Walter Wilcox, Terrence Draper, and Keh-Fei Liu, Chiral limit of nucleon lattice electromagnetic form-factors, Phys. Rev. D **46**, 1109 (1992).
[66] Andrei Alexandru, Manfried Faber, Ivan Horváth, and Keh-Fei Liu, Lattice QCD at finite density via a new canonical approach, Phys. Rev. D **72**, 114513 (2005).